Resource

Cell Reports

Transcriptomic Hallmarks of Tumor Plasticity and Stromal Interactions in Brain Metastasis

Graphical Abstract

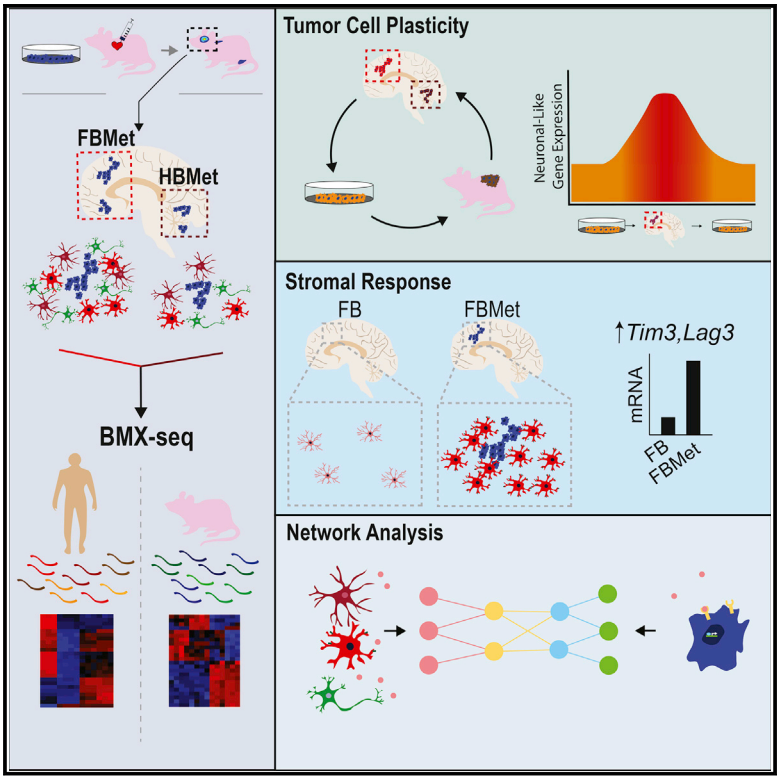

Authors

Emily Wingrove, Zongzhi Z. Liu, Kiran D. Patel, ..., Harriet M. Kluger, Veronica L. Chiang, Don X. Nguyen

Correspondence

don.nguyen@yale.edu

In Brief

Wingrove et al. develop an RNA-sequencing-based approach to distinguish the tumor versus stromal transcriptomes in brain metastasis. This reveals the molecular plasticity of malignant cells and the neuroinflammatory response of the stroma *in situ*. Common tumor-stromal gene networks are also identified across different tumor types that form brain metastasis.

Highlights

- BMX-seq reveals the tumor and stromal transcriptomes of brain metastasis *in situ*
- The brain microenvironment reversibly activates neuronal-like genes in tumor cells
- Increase of microglial-bound TIM3 is a neuroinflammatory marker of brain metastases
- Different cancers that form brain metastasis share common transcriptomic hallmarks

Wingrove et al., 2019, Cell Reports *27*, 1277–1292
April 23, 2019
https://doi.org/10.1016/j.celrep.2019.03.085

CellPress

Cell Reports
Resource

Transcriptomic Hallmarks of Tumor Plasticity and Stromal Interactions in Brain Metastasis

Emily Wingrove,[1,7] Zongzhi Z. Liu,[1,6,7] Kiran D. Patel,[1] Anna Arnal-Estapé,[1,5] Wesley L. Cai,[1] Mary-Ann Melnick,[5] Katerina Politi,[1,2,5] Cátia Monteiro,[4] Lucía Zhu,[4] Manuel Valiente,[4] Harriet M. Kluger,[2,5] Veronica L. Chiang,[3] and Don X. Nguyen[1,2,5,8,*]

[1]Department of Pathology, Yale University School of Medicine, New Haven, CT, USA
[2]Department of Medicine (Medical Oncology), Yale University School of Medicine, New Haven, CT, USA
[3]Department of Neurosurgery, Yale University School of Medicine, New Haven, CT, USA
[4]Brain Metastasis Group, Spanish National Cancer Research Center (CNIO), Madrid, Spain
[5]Yale Cancer Center, Yale University School of Medicine, New Haven, CT, USA
[6]Present address: Sema4, 333 Ludlow Street, South Tower 3rd Floor, Stamford, CT, USA
[7]These authors contributed equally
[8]Lead Contact
*Correspondence: don.nguyen@yale.edu
https://doi.org/10.1016/j.celrep.2019.03.085

SUMMARY

The brain is a major site of relapse for several cancers, yet deciphering the mechanisms of brain metastasis remains a challenge because of the complexity of the brain tumor microenvironment (TME). To define the molecular landscape of brain metastasis from intact tissue *in vivo*, we employ an RNA-sequencing-based approach, which leverages the transcriptome of xenografts and distinguishes tumor cell and stromal gene expression with improved sensitivity and accuracy. Our data reveal shifts in epithelial and neuronal-like lineage programs in malignant cells as they adapt to the brain TME and the reciprocal neuroinflammatory response of the stroma. We identify several transcriptional hallmarks of metastasis that are specific to particular regions of the brain, induced across multiple tumor types, and confirmed in syngeneic models and patient biopsies. These data may serve as a resource for exploring mechanisms of TME co-adaptation within, as well as across, different subtypes of brain metastasis.

INTRODUCTION

Metastases to the CNS are the most common intracranial malignancies. The incidence of CNS metastasis is rising due to increases in the number of patients with metastatic cancer, prolonged median duration of survival of these patients, and the limited efficacy of systemic and radiation therapies available to treat brain and leptomeningeal tumors (Valiente et al., 2018). CNS metastases are difficult to study because they are remarkably heterogeneous, varying both in their origin and in their location within different regions of the brain. In addition, unlike primary brain tumors from which brain tumor samples are often resected as part of treatment, tissue from brain metastases are difficult to obtain given that patients with widespread disseminated disease are less likely to undergo a craniotomy. The most common primary tumor types to spread to the CNS include melanoma, breast, and lung cancer (Kamar and Posner, 2010). Metastasis often forms within the brain parenchyma but may also develop in the dura and/or leptomeninges, either independently or in conjunction with intraparenchymal tumors (Takei et al., 2016). Finally, brain metastasis may present as a single tumor, oligometastases (2–4 tumor foci), or multiple metastases (>4 tumor foci) (Iuchi et al., 2015; Takei et al., 2016) with varying patterns of invasive outgrowth (Berghoff et al., 2013b; Kamp et al., 2018).

Although the cellular and genetic origins of various cancer subtypes that metastasize to the CNS are largely unique, the extent to which they share common or divergent molecular drivers of brain metastasis is less clear. The mechanisms by which cancers successfully seed and then grow in the brain may be influenced by genetic alterations, somatically acquired and selected for during tumor evolution (Brastianos et al., 2015). Moreover, the pathobiology of CNS metastases is also driven by adaptive mechanisms that can be instructed by disseminated tumor cells (DTCs) and/or their surrounding stroma. For instance, the blood-brain barrier (BBB) is a unique impediment to access the CNS from hematogenous circulation, and several molecular mediators of BBB extravasation overexpressed in metastatic tumor cells have been identified (Bos et al., 2009). Once in the brain parenchyma, stromal factors may dictate the adaptive responses of DTCs to enter reversible states of latency, survival, or proliferation (Kienast et al., 2010). One known source of such factors is the perivascular niche (Valiente et al., 2014).

Although brain metastases are generally poorly infiltrated by lymphocytes (tumor infiltrating lymphocytes [TILs]) (Berghoff et al., 2013a), this unique inflammatory milieu can be orchestrated by innate immune cells or resident glial cells. For instance, reactive astrocytes can initially limit the survival of DTCs before eventual co-option during later stages of micrometastatic outgrowth and drug resistance (Chen et al., 2016; Lee et al.,

2016; Lin et al., 2010; Priego et al., 2018). Furthermore, macrophages recruited from circulation or resident microglia can both be reprogrammed into what is referred to herein as tumor-associated macrophages (TAMs) that directly regulate DTC extravasation and outgrowth (Andreou et al., 2017; Sevenich et al., 2014). Microglia can initiate BBB leakage and are key mediators of neurodegeneration and intracerebral edema (Li and Barres, 2018; Urday et al., 2015). Perilesional edema is also a major complication for brain metastasis patients (Hanna et al., 2016; Ludwig et al., 2000; Stummer, 2007). The molecular determinants of glia-tumor interactions, neuroinflammation, and their consequences for brain metastasis-associated manifestations remain largely underexplored.

Recent methodological advances in the analysis of mammalian transcriptomes have improved our ability to accurately map species-specific gene transcripts of low abundance in tissues (Conway et al., 2012; Khandelwal et al., 2017). Here, we have improved on this approach to take advantage of human- and mouse-specific differences in the transcriptome of brain metastasis xenografts from multiple tumor types. As a result, we provide a comprehensive molecular portrait of intact brain metastases *in vivo*, while identifying co-adaptive molecular responses that occur specifically between tumor cells and the CNS stroma *in situ*.

RESULTS

Brain Metastasis Xenograft-RNA Sequencing

To perform a comprehensive transcriptomic analysis of metastatic tumor cells and stroma in the brain, we optimized an RNA-seq pipeline referred to here as brain metastasis xenograft-RNA sequencing (BMX-seq). BMX-seq was designed to map reads to the transcriptome of either human or mouse, and to compare brain metastases with normal brain tissue, subcutaneous tumors, and tumor cells in culture. BMX-seq maps each read to a merged genome and transcriptome, using uniquely mapped reads (to the mouse or human genome) for downstream analysis (Figure S1). We first utilized this approach for the analysis of the well-described human H2030-BrM3 cell model. The H2030-BrM3 cells are a sub-population of a prototypical lung adenocarcinoma (LUAD) cell line, H2030, which expresses a bioluminescent reporter and has undergone several rounds of selection *in vivo* for brain metastatic cells (Nguyen et al., 2009). H2030-BrM3 cells also encode few additional exonic mutations as compared with the H2030 parental line despite significant transcriptomic alterations (Jacob et al., 2015; Nguyen et al., 2009). When injected into the arterial circulation of athymic mice, H2030-BrM3 cells extravasate into the brain within 7 days, with perivascular micrometastasis (defined here as clusters <100 cells) detected between 7 and 21 days, and expansion as macrometastasis observed for up to 49 days (Stevens et al., 2017; Valiente et al., 2014).

As a first proof-of-principal experiment, H2030-BrM3 cells were injected either into the subcutaneous flank of athymic mice, into the arterial circulation, or seeded into standard monolayer cell culture conditions. Twenty-one days postinoculation, subcutaneous (s.c.) tumors, brain metastasis (BrMet), and cells passaged in culture (2D) were confirmed to be growing (Figures S2A and S2B) and were harvested for histological analysis and RNA extraction. Consistent with prior studies, diffusely invasive metastases in the brain parenchyma formed at this time point, whereas s.c. tumors from the same cell line were compact and well circumscribed with a typical LUAD histology (Figure 1A). Moreover, H2030-BrM3 cells formed distinct metastases in the forebrain and hindbrain of any given animal (Figures 1A and S2C), as is observed in human patients (Bender and Tomé, 2011). Thus, forebrain metastases (FBMets) and hindbrain metastases (HBMets) were macro-dissected separately. Non-tumor-bearing brain tissues from the corresponding forebrain (FB) or hindbrain (HB) region were harvested from sham-injected mice.

When analyzing bulk xenograft tissue, the reduction of false positive cross-mapped reads (e.g., mouse reads mistakenly mapped to the human transcriptome) is particularly important for accurate distinction of tumor versus stromal genes *in situ*. Therefore, we calculated the mapping accuracy of BMX-seq by using a subset of the reads from sham-injected brain tissue as a standard for true mouse reads and a subset of the reads from 2D tumor cell cultures as a standard for true human reads. BMX-seq results were also compared with the previously used Xenome method and an alternative mapping strategy based on Bowtie (ConBowtie). We found that the mapping quality of BMX-seq performs well based on the true positive (uniquely mapped) rate and the false positive (cross-mapping) rate (Figures 1B and 1C). Significantly, the BMX-seq workflow improved the cross-mapping accuracy by 85%–95% when compared with the other methods tested (Table S1).

Across all samples, approximately 75% of reads could be mapped to transcripts in the human or mouse genome (Figure S2D). Uniquely mapped reads in s.c. tumors aligned predominantly with human transcripts (77%), whereas fewer reads aligned to the murine genome (8%) (Figure 1D). Conversely, the transcriptome of forebrain metastasis and hindbrain metastasis tissue consisted of 5%–6% tumor-specific reads, whereas stromal reads accounted for the remaining bulk of the tissue (80%) (Figure 1D). These results are consistent with the tumor cell (human) or stromal (mouse) content of tumor-bearing tissues (Figure 1A). Roughly 13% of species-specific reads mapped to regions of the human or mouse genome that are currently unannotated (no features), whereas a very low percentage of mapped reads (1%–2%) aligned to regions with overlapping gene annotations (ambiguous) (Figure 1D). Despite different ratios of tumor or stroma across samples, a principal component analysis (PCA) revealed highly concordant tumor-specific (Figure 1E) and stromal-specific (Figure 1F) gene expression profiles that differentiated all experimental groups. Therefore, BMX-seq can distinguish tumor and stromal gene expression alterations from bulk xenograft tumor tissue at one of the earliest stages of metastatic outgrowth and in distinct regions of the brain.

Context-Dependent Transcriptomic Features of Brain Metastasis

As expected, global stromal gene expression in brain metastasis samples was significantly different from the stroma of s.c. tumors (Figure S2E). In agreement with recent studies, the stromal transcriptomes of our forebrain and hindbrain samples were

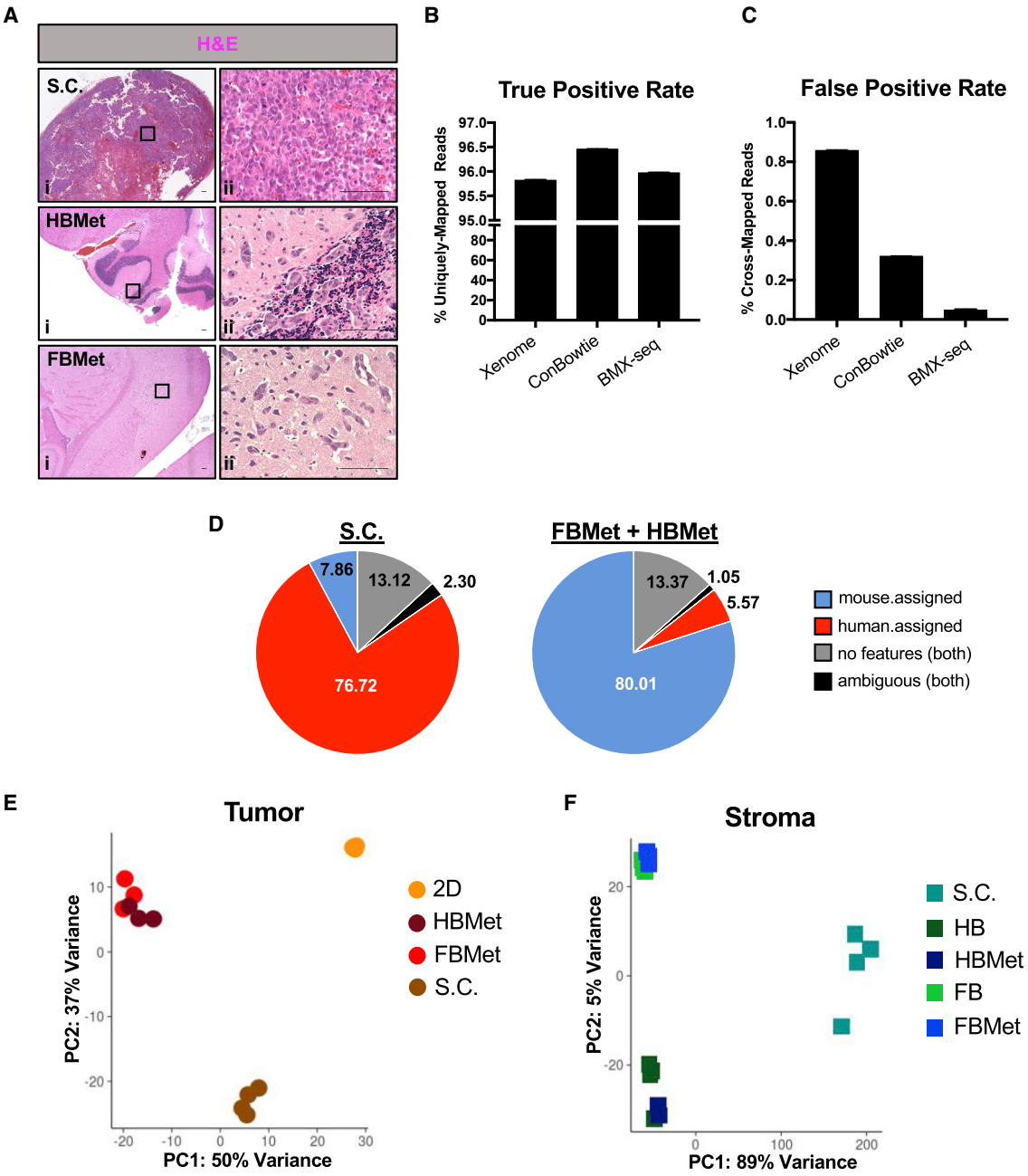

Figure 1. BMX-Seq Distinguishes the Transcriptomes of Tumor Cells and Stroma *In Vivo*

(A) H&E stains of subcutaneous (s.c.), hindbrain metastasis (HBMet), and forebrain metastasis (FBMet) tumors formed by injection of H2030-BrM3 cells. (i) ×4 images. (ii) ×40 magnification of boxes denoted in (i). Scale bars indicate 100 μm.

(B) Performance of BMX-seq mapping in discriminating human and mouse reads as compared with other pipelines (Xenome and ConBowtie). A subset of one million mouse and human reads was used to calculate the recovery rate (true positive rate) of real mouse and human reads mapped unambiguously and uniquely to either the mouse or human genome. Data are presented as a mean ± SD of 10 such subsets.

(C) The cross-mapping rate (false positive rate) of mouse and human reads erroneously mapped to either human or mouse genome was plotted as in (B).

(D) Pie charts demonstrating the percent of uniquely mapped reads in s.c. or brain metastasis (forebrain metastasis and hindbrain metastasis) tissue. Uniquely mapped reads were assigned to specific transcripts in the mouse genome (mouse.assigned), in the human genome (human.assigned), to regions without annotated exons (no features), or to regions annotated to multiple genes (ambiguous).

(E) Principle component analysis (PCA) comparing the gene expression profiles of H2030-BrM3 cells grown in culture (2D; n = 3), s.c. (n = 4), forebrain metastasis (n = 3), or hindbrain metastasis (n = 3) tumors.

(F) PCA of mouse gene expression profiles across the same samples in (E) and corresponding normal forebrain and hindbrain control regions. Forebrain and hindbrain control samples (n = 4).

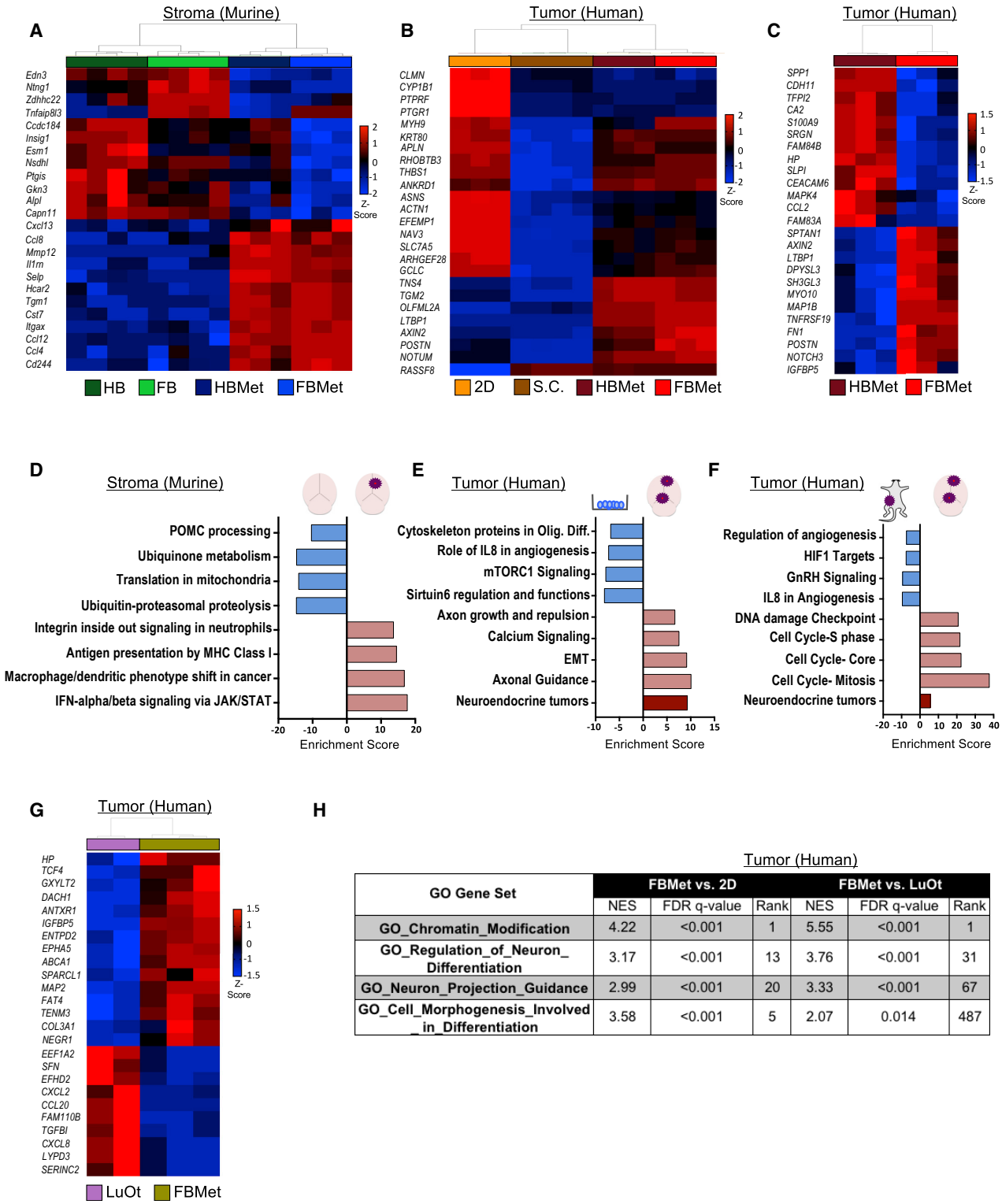

H

Tumor (Human)

GO Gene Set	FBMet vs. 2D			FBMet vs. LuOt		
	NES	FDR q-value	Rank	NES	FDR q-value	Rank
GO_Chromatin_Modification	4.22	<0.001	1	5.55	<0.001	1
GO_Regulation_of_Neuron_Differentiation	3.17	<0.001	13	3.76	<0.001	31
GO_Neuron_Projection_Guidance	2.99	<0.001	20	3.33	<0.001	67
GO_Cell_Morphogenesis_Involved_in_Differentiation	3.58	<0.001	5	2.07	0.014	487

Figure 2. Molecular Features of Tumor and Stroma during Brain Metastatic Colonization *In Vivo*

(A) Heatmap depicts hierarchical clustering of the top 24 genes similarly deregulated in the murine stroma when comparing tumor-bearing hindbrain and forebrain with their corresponding control regions. The 12 most upregulated and downregulated genes were filtered by adjusted p value < 0.05 and ranked by their average log2 fold change in both hindbrain metastasis (HBMet) and forebrain metastasis (FBMet) samples.

(legend continued on next page)

clearly distinguished by murine tissue signatures of the cerebellum, anterior cortex, or striatum of immune-competent mice (Figure S2F). However, when specifically comparing the stroma of forebrain metastasis or hindbrain metastasis with their corresponding regional control tissue (forebrain or hindbrain), significant alterations were detected that were commonly induced or suppressed in both tumor-bearing regions (Figure 2A). Analogously, the transcriptome of metastatic tumor cells in the brain was different from those of the same cells grown in culture or as s.c. tumors (Figure 2B). Moreover, the tumor cell transcriptomes of forebrain metastasis and hindbrain metastasis were highly similar, but not identical, with a subset of genes differentiating early-stage metastases in each region (Figure 2C).

To ascertain the biological significance of our BMX-seq results, we performed a comprehensive pathway analysis of the tumor and stromal transcriptomes separately. Pathways related to innate immune responses, such as macrophage function, were activated in the murine stroma of xenograft brain metastasis (Figure 2D). Pathways that were downregulated included ubiquitination pathways (Figure 2D). In comparison with the transcriptome of tumor cells grown in either region of the brain versus in culture, we observed tumor cell-specific upregulation of programs related to epithelial-to-mesenchymal transition (EMT), axonal guidance, and calcium signaling (Figure 2E). Brain metastatic H2030-BrM3 cells also had higher levels of cell-cycle-regulated genes and a similar increase in neuronal-like pathways as compared with s.c. tumors (Figure 2F; Table S2). Conversely, genes involved in angiogenesis and hypoxia were repressed (Figures 2E and 2F). We also compared brain metastasis tumors with lesions grown as orthotopic tumors in the lung (LuOt) (Figures 2G and S3A–S3C). We found many of the same networks to be preferentially enriched in H2030-BrM3 cells outgrowing in the brain versus the lung, including genes involved in chromatin modification, neuron projection, and neuron differentiation (Figure 2H).

Lineage Plasticity of Tumor Cells in the Brain

Epithelial lineage plasticity is believed to be a property of metastatic tumor cells from solid cancers. We observed variable expression of lineage-specific genes in brain metastatic tumor cells. For instance, in the brain tumor microenvironment (TME), H2030-BrM3 cells show increased expression of the epithelial marker *CDH1* despite elevated levels of transcription factors (e.g., *ZEB1*) and markers (e.g., *VIM*) of EMT (Figure 3A), potentially reflecting a ''partial'' EMT/MET phenotype (Chaffer et al., 2016). In addition, H2030-BrM3 cells in the brain display induced expression of CNS-enriched genes (e.g., *AKAP5*, *EFNB3*) and also preferentially activated lineage markers of neuroendocrine tumors (*NCAM1*) (Figure 3A) (Schleusener et al., 1996). Interestingly, many genes that are abundant in the CNS and are increased in brain-colonizing H2030-BrM3 cells encode for cell adhesion molecules (e.g., *CHL1*, *L1CAM*, *NCAM1*) (Katic et al., 2014; Maness and Schachner, 2007; Weledji and Assob, 2014; Williams and Barclay, 1988). Next, we performed a paracrine network analysis using differentially expressed brain stromal genes that encode for ligands or growth factors and their predicted activation of downstream target genes in tumor cells. The two most significant stromal-induced pathways in tumor cells (paracrine activated) were the Hippo pathway and canonical WNT/TCF signaling (Table S3; Figure 3B). The latter is consistent with increased expression of key WNT pathway components and target genes (e.g., *AXIN2*, *LGR6*, *CTNNB1*, *TCF4*) (Figure 3A) and the hypersensitivity of H2030-BrM3 cells to exogenous murine Wnt ligand stimulation (Nguyen et al., 2009).

We also evaluated whether the expression of certain lineage or pathway genes was permanent or reversible by isolating tumor cells from brain metastases, re-plating them in culture for three passages (forebrain metastasis→2D), and confirming tumor cell-specific gene expression by qPCR. TaqMan primers were verified as being species specific, and qPCR recapitulated the tumoral or stromal gene expression patterns observed by BMX-seq (e.g., *Postn*/*POSTN*; Figure S3D). This further illustrates that our approach can accurately differentiate tumor versus stromal gene expression. Both *AXIN2*, a marker of WNT activation, and *NCAM1* are highly induced in tumor cells by the brain TME, but their expression is reduced to near starting culture levels when tumor cells are removed from the brain and re-cultured at 70%–80% density (forebrain metastasis versus forebrain metastasis→2D; Figures 3C and 3D). In contrast, epithelial lineage markers such as *CDH1*

(B) Heatmap depicts hierarchical clustering of the top 25 most significant differentially expressed tumor genes in H2030-BrM3 cells under the indicated *in vitro* or *in vivo* conditions. Genes were ranked by adjusted p value.
(C) Heatmap depicts hierarchical clustering of the top 25 most significant differentially expressed tumor genes in forebrain metastasis compared with hindbrain metastasis samples. Genes were ranked by adjusted p value.
(D) Pathways most significantly dysregulated based on the differentially expressed stroma (murine) genes in forebrain metastasis versus control forebrain samples, as determined by Metacore analysis. Enrichment score, calculated as the $-\log_{10}$(p value) of plotted pathway maps and process networks, is plotted on the x axis. Bars represent deregulated pathway maps and process networks that are downregulated (blue) or upregulated (light red).
(E) Pathways most significantly dysregulated based on the differentially expressed tumor (human) genes in H2030-BrM3 cells grown in the brain (forebrain metastasis and hindbrain metastasis) versus the same cells grown in 2D. Enrichment score was calculated as in (D). Bar in dark red represents the enrichment score of neuroendocrine tumors plotted from the Diseases (by Biomarkers) grouping in Metacore.
(F) Pathways most significantly dysregulated in H2030-BrM3 cells grown in the brain (forebrain metastasis and hindbrain metastasis) versus the same cells grown as s.c. tumors. Enrichment score was calculated as in (D).
(G) Heatmap depicts hierarchical clustering of the top 25 most significant differentially expressed genes in H2030-BrM3 cells grown in the brain (forebrain metastasis) versus the same cells transplanted into the lungs to form orthotopic tumors (LuOt). Genes were ranked by adjusted p value.
(H) Pathways similarly enriched based on the differentially expressed tumor (human) genes in H2030-BrM3 cells grown in the brain versus the indicated samples. Normalized enrichment scores (NESs) and false discovery rate (FDR) q values computed by gene set enrichment analysis (GSEA).
See STAR Methods for further description.

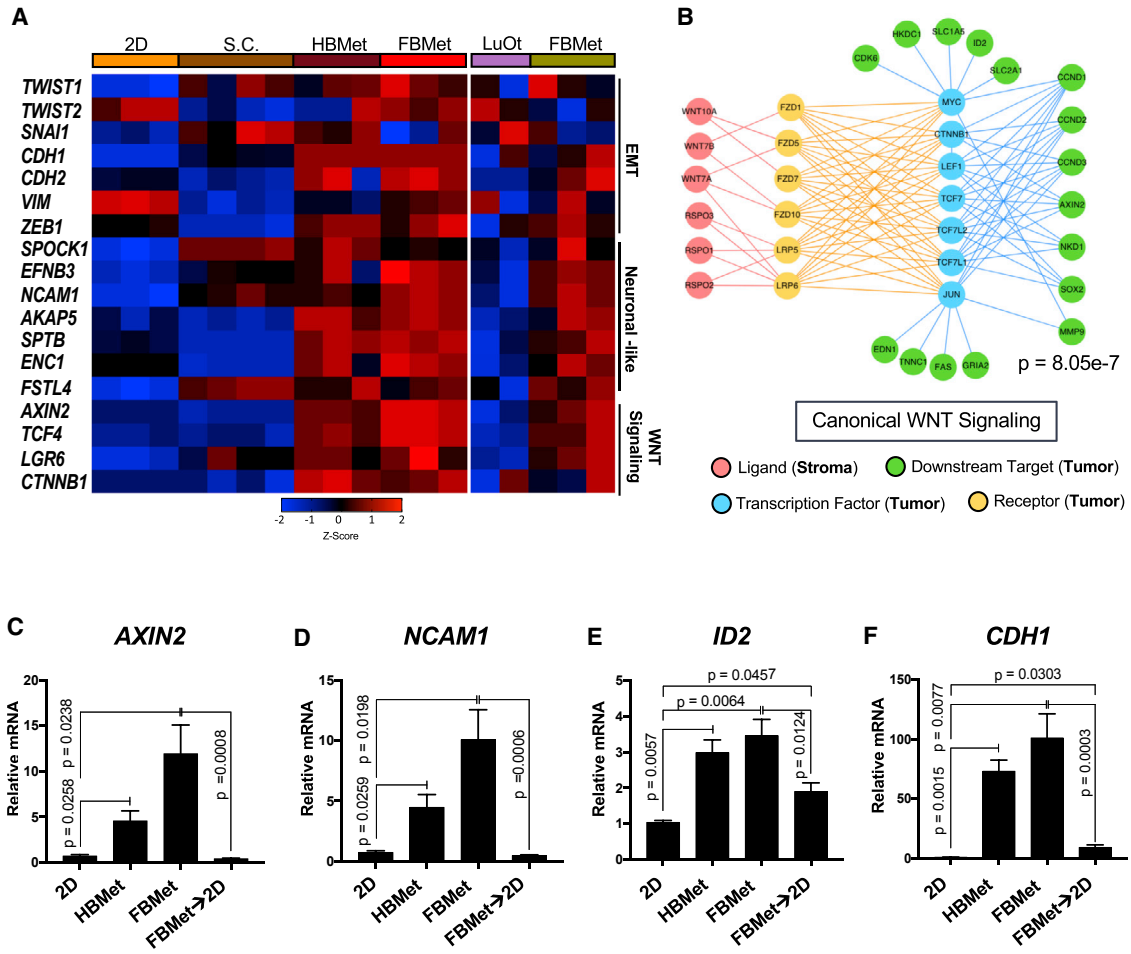

Figure 3. Adaptive Expression of Lineage-Specific Genes in Brain Metastatic Tumor Cells

(A) Heatmap depicts normalized expression of tumor genes associated with EMT, canonical WNT signaling, and neuronal-like pathways (from gene ontology [GO] gene sets Neuron_Projection_Guidance and Regulation_of_Neuron_Differentiation).

(B) A Stromal-Cancer Cell Crosstalk Network analysis identifies paracrine WNT signaling as being preferentially upregulated in tumor cells colonizing the brain. Red dots represent murine stromal ligands that are upregulated in forebrain metastasis versus in s.c. tumor samples; yellow dots represent receptors that are expressed in forebrain metastasis tumor cells; cyan dots represent pathway transcriptions factors expressed by forebrain metastasis tumor cells; and green dots represent downstream target genes upregulated in forebrain metastasis tumor cells.

(C–F) Tumor mRNA expression of (C) *AXIN2*, (D) *NCAM1*, (E) *ID2*, and (F) *CDH1* was measured using species-specific TaqMan qRT-PCR and normalized to *HPRT1* across all samples. H2030-BrM3 cells were grown in culture (2D; n = 3 samples) or *in vivo* as hindbrain metastasis (HBMet) (n = 3) or forebrain metastasis (FBMet) (n = 3). Forebrain metastases were also dissociated and re-plated in culture for three passages (FBMet → 2D; n = 2). Data are presented as mean ± SEM. p values are calculated by unpaired Student's t test. Comparisons that are not significant are not shown.

(epithelial) and *ID2* (stem cells) remain partially upregulated in tumor cells following seeding in the brain (Figures 3E and 3F). To determine whether the *in vitro* versus *in vivo* differences in gene expression were caused by cell density, we compared the mRNA levels of *AXIN2*, *NCAM1*, and *CDH1* in H2030-BrM3 cells cultured between 10% and 80% confluency (Figure S3E). Expression of these lineage or pathway genes was not significantly influenced by cell density unless cultured at very low confluency (10%), which causes gene repression (Figure S3F), whereas these genes are activated in diffuse invasive lesions *in vivo*. We conclude that the brain stromal TME induces adaptive transcriptomic programs that can either be reversed or partially sustained in tumor cells.

Neuroinflammatory Response of the Brain Metastatic Stroma

Next, we interrogated the brain metastasis stromal transcriptome for the expression of previously defined gene signatures of known CNS cell types (Zhang et al., 2014). In the brain metastatic stroma, genes associated with astrocytes and microglia were enriched (Figure S4A). This was supported by qPCR of *Gfap* and *C1qb* (Figure 4A), markers of activated astrocytes and brain TAMs, respectively (Bowman et al., 2016; Pekny and Nilsson, 2005). The brain metastatic stroma expressed well-established pro-inflammatory cytokine genes (*Il1a*, *Il1b*), markers of macrophage phagocytosis (*Cd68*), genes involved in oxidative stress (*Ncf1*, *Cyba*), and markers of immune-suppression or

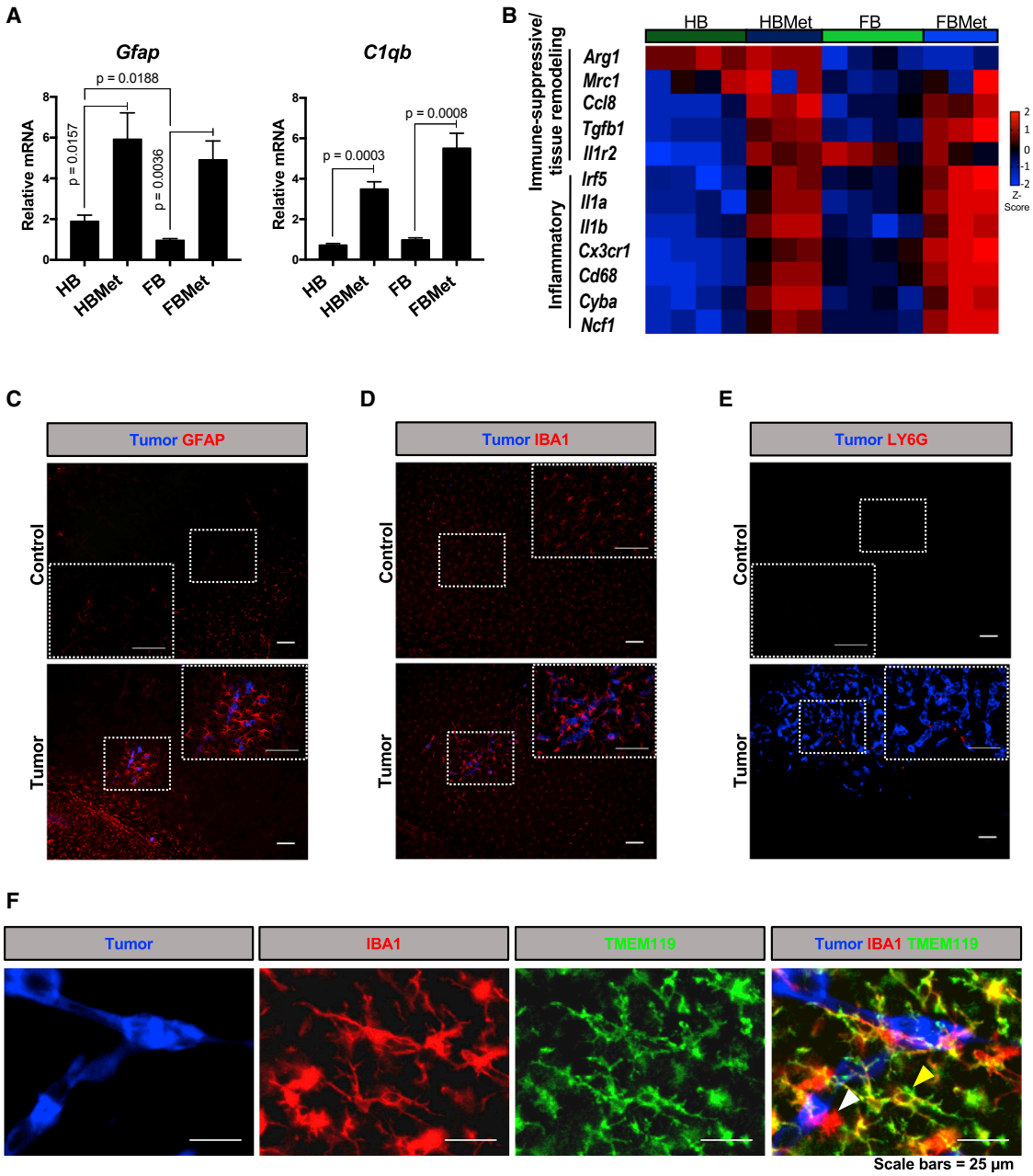

Figure 4. Adaptive Neuroinflammatory Response in the Brain Metastatic Stroma

(A) Stromal mRNA expression of known genes expressed in astrocytes (*Gfap*) and macrophages (*C1qb*) using species-specific TaqMan qRT-PCR. Data were normalized to *Hprt* across all samples. Data are presented as mean ± SEM. p values are computed by unpaired Student's t test. Forebrain metastasis (FBMet) and hindbrain metastasis (HBMet) (n = 3); hindbrain (HB) and forebrain (FB) (n = 4). Comparisons that are not significant are not shown.

(B) Heatmap depicts normalized expression values of stromal genes associated with pro-inflammatory or immune-suppressive or tissue remodeling functions as determined by current literature.

(C–E) Representative images of immunofluorescent (IF) staining of astrocytes (C; GFAP; red), TAMs (D; IBA1; red), neutrophils (E; LY6GG; red), and tumor cells (GFP; blue) in tumor-bearing brain (bottom) and in corresponding control regions (top).

(F) Representative IF staining of microglia (TMEM119; green), TAMs (IBA1; red), and tumor (GFP; blue) in the metastatic brain. Yellow arrow indicates a TMEM119-positive, IBA1-positive cell. White arrow indicates TMEM119-negative, IBA1-positive cell.

Scale bars are 100 μm except where otherwise indicated.

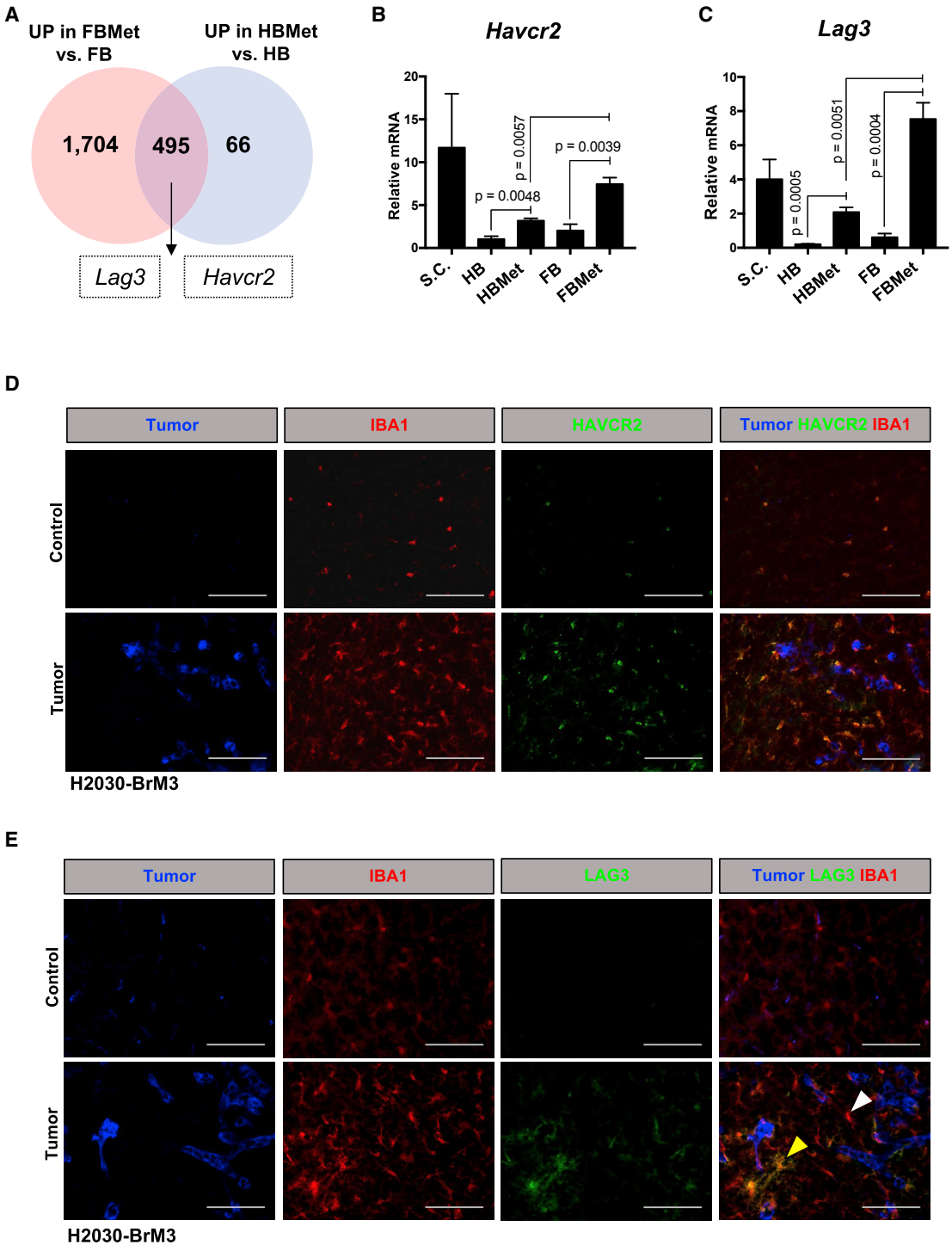

Figure 5. LAG3 and HAVCR2 Are Upregulated in TAMs in the Brain Metastatic Niche

(A) Venn diagram shows the number of stromal genes similarly upregulated in forebrain metastasis (FBMet) and hindbrain metastasis (HBMet) versus in their corresponding control brain regions (forebrain [FB] and hindbrain [HB]). Cutoff for significantly upregulated genes was an adjusted p value < 0.05 for the comparisons in question. Genes with an average reads per kilobase of transcript per million mapped reads (RPKM) <1.0 were excluded.

(B) mRNA expression of *Havcr2* measured using species-specific TaqMan qRT-PCR across the indicated samples and normalized to stromal *Hprt*. Forebrain metastasis and hindbrain metastasis (n = 3); hindbrain and forebrain (n = 4); s.c. (n = 4).

(C) mRNA expression of *Lag3* measured using species-specific TaqMan RT-qPCR across the indicated samples and normalized to stromal *Hprt*. Forebrain metastasis and hindbrain metastasis (n = 3); hindbrain and forebrain (n = 4); s.c. (n = 4).

(legend continued on next page)

tissue remodeling (*Ccl8*, *Tgfb1*) (Figure 4B). Notably, *Hepatitis A virus cellular receptor 2 (Havcr2*, also known as *Tim-3*) was induced in tumor-bearing stroma (Figure S4B). *Havcr2* is an immunosuppressive marker when expressed in T cells (Anderson et al., 2016) but is conversely a pro-inflammatory marker when expressed in monocytes and activated microglia (Anderson et al., 2007; Koh et al., 2015; Xu et al., 2013). Although expressed at low levels, increases in the neutrophil chemotactic receptor gene *Cxcr2* (Cacalano et al., 1994) were observed (Figure S4B). Interestingly, the expression of several innate immune receptors in the stroma correlated with increased expression of their ligands in metastatic tumor cells. Two examples are *LGALS9* and *CXCL7* (Figure S4C), which are ligands for *Havcr2* and *Cxcr2*, respectively (Stillie et al., 2009; Zhu et al., 2005). As such, BMX-seq may also reveal tumor-derived paracrine signals to the stroma.

To determine whether the stromal predictions by BMX-seq correlate with actual stromal cell content, we performed immunofluorescent (IF) staining on time-matched tissue sections. IF staining confirmed a strong enrichment of glial fibrillary acidic protein (GFAP)-positive reactive astrocytes surrounding micrometastases (Figure 4C, bottom). Likewise, an increase in IBA1-positive TAMs (Streit et al., 2009; Zhang et al., 2014) was readily detected peritumorally with individual TAMs also infiltrating metastatic lesions (Figure 4D, bottom) in comparison with control regions where microglia were sparse (Figure 4D, top). TAMs displayed cellular features of microglial activation including larger soma size and a transition from ramified to more amoeboid-like morphology (Figure 4D, bottom). Furthermore, in this model, most IBA1-positive TAMs co-expressed the microglia-enriched marker TMEM119 (Bennett et al., 2016) (Figure 4F). Although neutrophils were less abundant in the brain TME at this early stage, we also confirmed their recruitment (Figure 4E, bottom). To determine whether these observations were relevant in an immunocompetent setting, we derived a syngeneic brain metastatic cell population (368T1-Br) by *in vivo* selection using a tumor cell line from a $KRAS^{G12D}$; $p53^{-/-}$ mutant genetically engineered mouse model of LUAD (Winslow et al., 2011). Twenty-one days after metastatic outgrowth in the brain of B6129SF1/J syngeneic mice, brain metastasis tissue was collected (Figure S4D). IF staining confirmed GFAP-, IBA1-, and LY6G-positive stromal cell recruitment in areas directly surrounding tumor lesions (Figures S4E and S4G), with IBA1-positive TAMs also infiltrating large tumors (Figure S4F; bottom).

In addition to *Havcr2*, BMX-seq identified *Lymphocyte activation gene 3* (*Lag3*) as being increased in the stroma of forebrain metastases and hindbrain metastases compared with their normal brain regions (Figures 5A–5C). Similar to HAVCR2, LAG3 is thought to be expressed on lymphocytes and functions as an immunosuppressive checkpoint receptor (Anderson et al., 2016). Although *Havcr2* and *Lag3* were expressed in the stroma surrounding s.c. tumors, their induction in the brain TME is notable because it has been suggested that HAVCR2 and LAG3 may be expressed on microglia (Bennett et al., 2016; Gautier et al., 2012), whereas LAG3 may also be expressed by neurons (Mao et al., 2016). In brain metastasis from the H2030-BrM3 model, expression of LAG3 and HAVCR2 was increased in areas within and directly surrounding metastatic lesions (Figures 5D and 5E) as compared with control brain regions. HAVCR2 expression overlapped with the TAM marker IBA1 (Figure 5D). Likewise, LAG3 expression overlapped with IBA1 (Figure 5E) and microglial marker TMEM119, but not with markers of astrocytes or neurons (Figure S5A). Finally, these observations were recapitulated in the immune-competent 368T1-Br model (Figures S5B–S5D). We conclude that the identification of inflammatory markers and co-adaptive enrichment of various stromal cell types in the brain metastatic TME can be inferred by performing BMX-seq on bulk tissue.

Transcriptomic Hallmarks of Brain Metastases across Primary Tumor Types and Models

Regions in the forebrain (e.g., cerebrum) are the most common site of brain metastases (Bender and Tomé, 2011; Delattre et al., 1988). Three major sources of human forebrain metastases are lung cancer, melanoma, and breast cancer. The extent to which these diseases share common or divergent mechanisms of tumor-stromal co-adaptation in the forebrain is not clear. We therefore performed BMX-seq, directly comparing our LUAD model with well-characterized xenograft models of brain metastasis from triple-negative breast cancer (MDA-MB-231 BrM2; referred to here as MDA231-BrM2) and melanoma (A375-Br). These models have undergone *in vivo* selection in a manner similar to the H2030-BrM3 cells (Bos et al., 2009; Xie et al., 2006). To control for regional differences in the CNS, all three cell lines were injected directly into the forebrain of athymic mice with sham forebrain injections included as controls for normal tissue (Figures S6A and S6B). In parallel, metastatic cells were seeded into monolayer culture. Cells in culture, brain metastases, and control tissue were then harvested when brain tumor burden was similar (14–21 days postinjection).

BMX-seq mapping results were highly consistent across all models (Figures S6C and 6D). Moreover, the growth pattern, as well as 57% of the transcriptomic differences observed in the H2030-BrM3 intra-cranial model compared with cells growing in monolayer, were concordant to those obtained following intra-arterial injection (Figures S6E–S6I). When directly comparing the lung, melanoma, and breast models with each other, major differences in the tumor cell transcriptome across disease types (Figure S6J) and *in vivo* versus *in vitro* conditions were observed, with H2030-BrM3 cells having the most molecular alterations once in the brain TME (Figure 6A). Nevertheless, a significant number of adaptive responses were

(D) Representative IF staining of HAVCR2 (green), TAMs (IBA1; red), and tumor (GFP; blue) in an area directly surrounding brain metastatic tumor (bottom), as well as in corresponding control regions (top).

(E) Representative IF staining of LAG3 (green), TAMs (IBA; red), and tumor (GFP; blue) in tumor-bearing brain (bottom) and in the corresponding control regions (top). Yellow arrow indicates LAG3, IBA1-positive cell; white arrow indicates LAG3-negative, IBA1-positive cell.

Scale bars, 100 μm. qRT-PCRs are presented as mean ± SEM. p values are computed by unpaired Student's t test. Comparisons that are not significant are not shown.

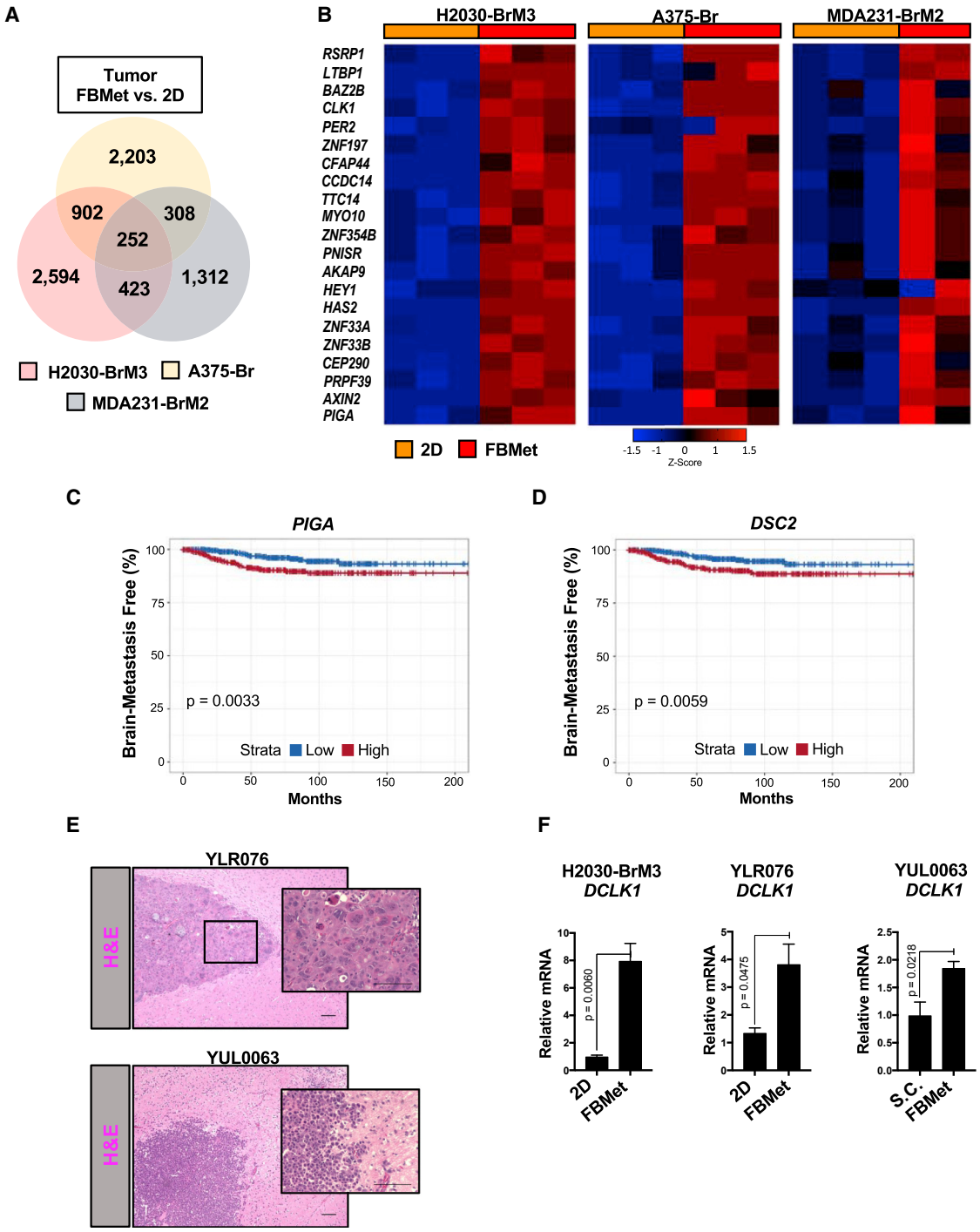

Figure 6. Conserved Transcriptomic Hallmarks across Human Models of Brain Metastasis

(A) Venn diagram comparing tumor (human) (forebrain metastasis (FBMet) versus 2D) genes that are differentially expressed across models of brain metastasis. Cutoff for significant differentially regulated gene was an adjusted p value < 0.05 for the comparison in question. Genes with an average RPKM <1.0 were excluded.

(B) Three heatmaps depict normalized expression of genes that are significantly upregulated in forebrain metastasis tumors across different disease models. Gene expression values are normalized to the 2D samples of each given tumor type. Cutoff was an adjusted p value < 0.05 for the comparison in question.

(C) Human breast tumors from independent institutes were compiled and classified as "high" or "low" based on whether expression of *PIGA* was above or below the median, respectively. Kaplan-Meier curves were generated for the incidence of brain relapse of median "high" versus "low" groups. p value was calculated by log rank test. n = 855.

(D) Analysis was done as in (C) for gene *DSC2*.

(legend continued on next page)

shared, including 252 genes that were dysregulated in the tumor cells of all three models (Figure 6A; Table S4), whereas 1,633 genes were similarly dysregulated in two out of the three models, such as the CNS-enriched kinase *DCLK1*. Core tumor adaptive responses across all three disease models were enriched for genes involved in the canonical WNT pathway activation (*AXIN2*), genes that are CNS enriched (*HEY1*), and genes involved in cell motility (*CFAP44*, *CEP290*) (Figure 6B). When comparing forebrain metastases with s.c. tumors, we also validated that *AXIN2* is preferentially expressed in forebrain metastases across disease models, whereas *HEY1* was increased *in vivo* but more preferentially induced in forebrain metastases from lung cancer and melanoma (Figure S7A). Of this core response, some genes involved in cell adhesion (*DSC2*) (Koch and Franke, 1994) and neuronal development (*PIGA*) (Yuan et al., 2017) (Table S4) were differentially expressed in human primary breast tumors, and their upregulation correlates with an increased incidence of brain relapse (Figures 6C and 6D).

Gene set enrichment analysis also revealed common upregulation of genes involved in cell projection assembly across all models and particular enrichment of neuronal-related pathways in brain metastases derived from breast and lung cancer cells (Table S6). To ascertain whether the induced expression of neuronal-like genes was conserved in more recently generated models of human lung cancer metastasis, we performed species-specific qPCR using patient-derived xenografts (PDXs) from brain metastasis biopsies. YLR076 was derived from the brain metastasis of a patient with squamous cell carcinoma and is capable of growing in monolayer culture or as brain metastases (Figure 6E, top). YUL0063 originated from the brain metastasis of a neuroendocrine carcinoma patient and was maintained *in vivo* as s.c. tumors or brain metastases (Figure 6E, bottom). Using these PDX models and the H2030-BrM3 lung cancer model, we confirmed that the CNS-enriched gene *DCLK1* was increased in cells within the brain TME relative to lung tumor cells grown in culture or in the flank of mice (Figure 6F).

BMX-seq also revealed a significant number of divergent transcriptional changes in the stroma of each disease subtype, with the lung and breast cancer forebrain metastasis models sharing the most similar stromal responses (Figures 7A and S7B). Twenty-eight stromal genes were differentially expressed in all three models in comparison with control forebrain (Figure 7A; Table S5). This core stromal adaptive response included markers of reactive astrocytes (*Gfap*) and TAMs (*Ctss*, *C1qb*, *Ly86*, and *Lag3*) (Figure 7B). Of these genes, we tested *C1qb* by qPCR and confirmed it to have increased expression in the stroma of brain metastases (Figure 7C). *Lag3* was induced in the bulk tissue of all three disease models, whereas *Havcr2* was more significantly upregulated in brain metastasis tissue from models of lung and breast cancer (Figure 7B). However, IF staining revealed IBA1-positive TAMs, both within and surrounding brain metastases, that were LAG3- and HAVCR2-positive in all three disease models and the two PDXs tested in this study (Figures 7D, 7E, S7C, and S7D). Thus, although neuroinflammation may vary in magnitude and localization, it occurs across brain metastasis models. Finally, we obtained tissue from the original patient biopsy used to establish PDX YLR076. We also collected additional human brain metastatic biopsies from craniotomies performed on patients with melanoma or non-small-cell lung cancer (NSCLC; sarcomatoid subtype). In two of the three cases, specific HAVCR2 expression was detected within the tumor compartments, which is in agreement with prior studies (Su et al., 2018; Wiener et al., 2007; Zhang et al., 2017; Zhuang et al., 2012) (Figures 7F and 7H). Despite variable staining of tumor cells, brain stromal HAVCR2 expression was significantly, although not exclusively, co-expressed on infiltrating IBA-positive TAMs in all three cases (Figures S7E–S7G and 7F–7H).

In summary, our BMX-seq approach generated a comprehensive transcriptomic portrait of brain metastases *in vivo* and provides a biologically relevant platform to discover mechanisms of tumor-stroma co-adaptation across different models and subtypes of brain metastasis. These data can be explored by the research community via an interactive web portal (http://bmxexplorer.gotdns.org/).

DISCUSSION

To date, several allograft and xenograft models have been generated that not only recapitulate brain metastasis, but also enable the quantification of the early steps of metastatic outgrowth (Bos et al., 2009; Nguyen et al., 2009; Winslow et al., 2011; Xie et al., 2006). Using such models, certain molecular mechanism(s) of CNS metastasis have been discovered by an *a priori* determination of the tumor and stromal cell types of interest. Each cell type is then dissociated from bulk tumor tissue for molecular analysis. Although useful, these strategies require significant optimization of cell isolation steps and may preclude the identification of molecular responses that are induced as malignant cells adapt to the TME *in situ*. One method to molecularly profile tumor-specific gene responses without cell isolation is translating ribosome affinity purification (TRAP) (Doyle et al., 2008), which requires genetic modification of the tumor cells beforehand and purification of specific mRNAs (Zhang et al., 2013). In principal, xenograft tissue can be directly leveraged to distinguish tumor cell from stromal gene responses *in situ*, and prior transcriptomic analyses from these models have been performed with species-specific microarrays (Park et al., 2011; Sevenich et al., 2014). We developed a complementary and comprehensive RNA-seq-based approach, which improves the sensitivity and accuracy of mapping mammalian transcripts.

BMX-seq enabled us to distinguish transcriptomic alterations in an invasive multi-focal brain metastasis model at one of the earliest stages of colonization and within particular regions of the brain. There are obvious limitations to xenografts, which

(E) H&E stains of forebrain metastases formed 21–48 days after intra-cranial injection of tumor cells from PDXs YLR076 (top) and YUL0063 (bottom).
(F) mRNA expression of *DCLK1* as measured by species-specific TaqMan qRT-PCR across the indicated H2030-BrM3 and PDX samples. Gene expression normalized to human *HPRT1* (H2030-BrM3 and YLR076) or human *ACTB* (YUL0063). H2030 BrM3 forebrain metastasis (n = 3); YUL0063 forebrain metastasis and s.c. (n = 4); YLR076 forebrain metastasis (n = 5); and H2030-BrM3 and YLR076 2D (n = 3).
See STAR Methods for further characterization of PDXs. Data are presented as mean ± SEM. p values are computed by unpaired Student's t test.

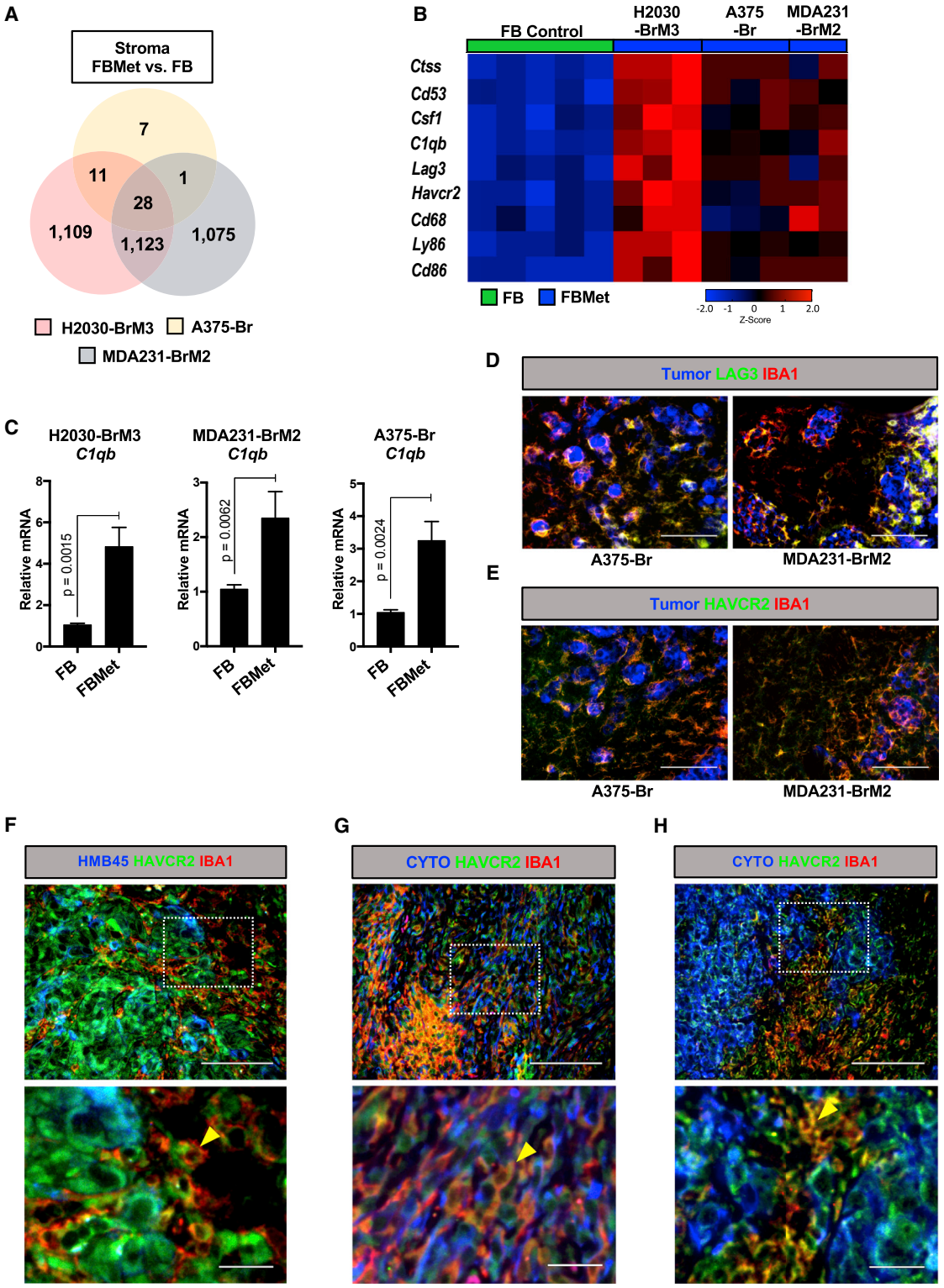

Figure 7. Conserved Inflammatory Response of the Stromal Microenvironment during Brain Metastasis

(A) Venn diagram comparing stroma (murine) (forebrain metastasis [FBMet] versus forebrain [FB]) genes that are differentially expressed across models of brain metastasis. Cutoff for significant differentially regulated gene was an adjusted p value < 0.05 for the comparison in question. Genes with an average RPKM < 1.0 were excluded.

(legend continued on next page)

lack an adaptive immune system and may not recapitulate certain paracrine interactions because of incompatibilities between human cells and a murine host. Our comparisons were also limited to three major models using an approach that may not be conducive for the identification of somatic mutations in human brain metastases. Nevertheless, several of our transcriptomic findings were conserved across patient-derived models and a syngeneic mouse model of brain metastasis, attesting to the biological relevance and utility of this approach as a platform for discovery. We uncovered adaptive tumor cell responses that were either unique or conserved across several commonly used models of brain metastasis. Transcriptomic responses shared by metastatic cells from lung cancer, breast cancer, and melanoma included upregulation of pathways involved in WNT signaling and cell motility, as well as genes enriched in neuronal and glial cell types. Activation of axon guidance and synaptogenesis genes by brain metastatic cells was reported in previous studies (Park et al., 2011; Sato et al., 2017). Notably, our analysis confirmed upregulation of genes such as SERPINI1 and L1CAM, previously shown to mediate brain metastasis (Valiente et al., 2014). Interestingly, we demonstrate that some of the tumor cell adaptive gene responses, including those involved in neuronal pathways, are reversible. Collectively, these findings highlight the remarkable lineage plasticity of metastatic cells in the brain. This plasticity is likely to be epigenetically instructed by the brain TME. Understanding the mechanisms underlying these reversible programs may provide novel avenues for therapeutic intervention in addition to targeting recurrent driver mutations in human brain metastasis.

Although brain metastases may have low counts of TILs (Berghoff et al., 2013a), recent studies illustrate the power of harnessing immunotherapies for clinical benefit in patients with CNS metastasis (Goldberg et al., 2016). In addition, the contribution of innate immunity and pro-inflammatory cells in brain metastasis remains poorly characterized. Despite the analysis of bulk tumor tissue, BMX-seq can accurately generate insights into alterations of the inflammatory stroma. Our approach predicted the enrichment of astrocytes and TAMs surrounding and infiltrating metastatic lesions, and the co-adaptive molecular alterations that could be driven by tumor cells. Surprisingly, the three models tested herein displayed a significant number of transcriptomic differences in their stroma, even when accounting for the host strain, sex, and site of tumor cell growth. The heterogeneity of stromal cells in the brain TME is also reflected in the concomitant activation of pro-inflammatory and tissue repair or immunosuppressive markers in brain metastasis tissue, which may be due to a spectrum of myeloid cell polarization states (Kiss et al., 2018) in the context of the brain TME.

Surprisingly, we detected robust *Lag3* and *Havcr2* induction in metastasis-bearing stroma of immunocompromised mice devoid of T cells, as well as in immunocompetent syngeneic animals. Although these receptors are expressed on immunosuppressed lymphocytes in many extra-cranial tissues, we found LAG3- and HAVCR2-positive cells in the brain TME to include TAMs and, more specifically, microglia. This observation was also intimated by RNA-seq analysis of isolated microglia (Bennett et al., 2016). The expression of such immune receptors on TAMs may functionally contribute to brain metastasis progression or could be a collateral effect of reactive neuroinflammation. The latter is also clinically significant because it is linked to peri-tumoral edema and neurological complications, which have historically excluded brain metastasis patients from clinical trials (Stummer, 2007). Future studies to distinguish between these possibilities will be of interest.

The incidence of CNS metastases in human cancers is on the rise. There is an imminent need to understand the molecular pathogenesis of brain metastasis progression and how the interaction between these tumors and the brain TME causes its associated morbidity. Our study provides a robust, tractable, and sensitive RNA-seq-based approach to map the transcriptomic hallmarks of both tumor cells and the stroma within the brain metastatic niche. This approach and its ensuing dataset can be used as a resource to guide further studies on the biology of CNS metastasis.

STAR★METHODS

Detailed methods are provided in the online version of this paper and include the following:

- KEY RESOURCES TABLE
- CONTACT FOR REAGENT AND RESOURCE SHARING
- EXPERIMENTAL MODEL AND SUBJECT DETAILS
  - Primary Cell Culture
  - Mice
  - Patient Derived Xenografts
  - Additional Human Tissue

(B) Heatmap depicts normalized expression of stromal genes enriched in TAMs and significantly upregulated in forebrain metastasis versus forebrain samples across at least two disease models.
(C) mRNA expression of stromal *C1qb* across forebrain metastasis (n = 2–3) and forebrain (n = 5) samples. Expression normalized to stromal *Hprt*. p values are computed by unpaired Student's t test. Data are presented as mean ± SEM.
(D) Representative IF staining of LAG3 (green), TAMs (IBA1; red), and tumor cells (A375-Br = GFP; MDA231-BrM2 = human-specific vimentin; blue) in tumor-bearing brains. Scale bars, 100 μm.
(E) Representative IF staining of HAVCR2 (green), TAMs (IBA1; red), and tumor cells (A375-Br, MDA231-BrM2 = GFP; blue) in tumor-bearing brains. Scale bars, 100 μm.
(F) Representative IF staining of HAVCR2 (green), TAMs (IBA1; red), and tumor cells (HMB45; blue) in human brain metastasis sample BMTP6 (melanoma). Yellow arrow indicates IBA1-positive, HAVCR2-positive cell.
(G) Representative IF staining of HAVCR2 (green), TAMs (IBA1; red), and tumor cells (Pan-Cytokeratin; blue) in human brain metastasis sample VC004 (NSCLC). Yellow arrow indicates IBA1-positive, HAVCR2-positive cell.
(H) Representative IF staining of the original tumor biopsy of YLR076 (squamous carcinoma). Tumor (Pan-Cytokeratin; blue), TAMs (IBA1; red), and HAVCR2-positive cells (green) were stained. Yellow arrow indicates IBA1-positive, HAVCR2-positive cell. Scale bars, 100 μm (top); 25 μm (bottom).

SUPPLEMENTAL INFORMATION

Supplemental Information can be found online at https://doi.org/10.1016/j.celrep.2019.03.085.

ACKNOWLEDGMENTS

We thank Sally Adua for critical review of the manuscript. This work was funded by grants R01CA166376, R01CA191489, and W81XWH-15-1-0117 and the Beatrice Kleinberg Neuwirth Fund (to D.X.N.); Yale Lung Cancer SPORE grant P50CA196530 (to K.P. and D.X.N.); Yale SPORE in Skin Cancer grants P50 CA121974, K24CA172123, and R01 CA216846 (to H.M.K.); MINECO grants SAF2017-89643-R and SAF2015-62547-ERC, Bristol-Myers Squibb-MRA Young Investigator Award 2017, Fundación Ramón Areces, and CLIP CRI Award 2018 (to M.V.); La Caixa-Severo Ochoa International PhD Program Fellowship (to L.Z.); and FCT PhD Fellowship SFRH/BD/100089/2014 (to C.M.). M.V. is a Ramón y Cajal Investigator (RYC-2013-13365) and member of EMBO YIP (4053). K.D.P. was supported by grant T32 CA193200, W.L.C. by grant DGE-1122492, and E.W. by grant T32 GM100884.

AUTHOR CONTRIBUTIONS

Conceptualization: E.W., Z.Z.L., and D.X.N.; Methodology: E.W., Z.Z.L., and D.X.N.; Investigation: E.W., Z.Z.L., K.D.P., A.A.-E., M.-A.M., L.Z., C.M., and V.L.C.; Analysis: E.W., Z.Z.L., W.L.C., and D.X.N.; Writing: E.W., Z.Z.L., K.P., A.A.-E., K.D.P., H.M.K., M.V., V.L.C., and D.X.N.; Supervision: M.V., K.P., and D.X.N.

DECLARATION OF INTERESTS

D.X.N. received research funding from AstraZeneca. K.P. received research funding from AstraZeneca, Kolltan, Roche, and Symphogen, as well as personal fees from Takeda, NCCN, Novartis, Merck, AstraZeneca, Tocagen, Maverick Therapeutics, and Dynamo Therapeutics. K.P. is co-inventor on a patent licensed to Molecular MD for EGFR T790M mutation testing (through MSKCC). H.M.K. received research funding from Merck, Bristol-Myers Squibb, and Apexigen, as well as personal fees from Regeneron, Alexion, Prometheus, Corvus, Nektar, Biodesix, Roche-Genentech, Pfizer, Iovance, Immunocore, and Celldex.

Received: May 26, 2018
Revised: November 6, 2018
Accepted: March 22, 2019
Published: April 23, 2019

REFERENCES

Anderson, A.C., Anderson, D.E., Bregoli, L., Hastings, W.D., Kassam, N., Lei, C., Chandwaskar, R., Karman, J., Su, E.W., Hirashima, M., et al. (2007). Promotion of tissue inflammation by the immune receptor Tim-3 expressed on innate immune cells. Science *318*, 1141–1143.

Anderson, A.C., Joller, N., and Kuchroo, V.K. (2016). Lag-3, Tim-3, and TIGIT: Co-inhibitory Receptors with Specialized Functions in Immune Regulation. Immunity *44*, 989–1004.

Andreou, K.E., Soto, M.S., Allen, D., Economopoulos, V., de Bernardi, A., Larkin, J.R., and Sibson, N.R. (2017). Anti-inflammatory Microglia/Macrophages As a Potential Therapeutic Target in Brain Metastasis. Front. Oncol. *7*, 251.

Bender, E.T., and Tomé, W.A. (2011). Distribution of brain metastases: implications for non-uniform dose prescriptions. Br. J. Radiol. *84*, 649–658.

Bennett, M.L., Bennett, F.C., Liddelow, S.A., Ajami, B., Zamanian, J.L., Fernhoff, N.B., Mulinyawe, S.B., Bohlen, C.J., Adil, A., Tucker, A., et al. (2016). New tools for studying microglia in the mouse and human CNS. Proc. Natl. Acad. Sci. USA *113*, E1738–E1746.

Berghoff, A.S., Lassmann, H., Preusser, M., and Höftberger, R. (2013a). Characterization of the inflammatory response to solid cancer metastases in the human brain. Clin. Exp. Metastasis *30*, 69–81.

Berghoff, A.S., Rajky, O., Winkler, F., Bartsch, R., Furtner, J., Hainfellner, J.A., Goodman, S.L., Weller, M., Schittenhelm, J., and Preusser, M. (2013b). Invasion patterns in brain metastases of solid cancers. Neuro-oncol. *15*, 1664–1672.

Bos, P.D., Zhang, X.H., Nadal, C., Shu, W., Gomis, R.R., Nguyen, D.X., Minn, A.J., van de Vijver, M.J., Gerald, W.L., Foekens, J.A., and Massagué, J. (2009). Genes that mediate breast cancer metastasis to the brain. Nature *459*, 1005–1009.

Bowman, R.L., Klemm, F., Akkari, L., Pyonteck, S.M., Sevenich, L., Quail, D.F., Dhara, S., Simpson, K., Gardner, E.E., Iacobuzio-Donahue, C.A., et al. (2016). Macrophage Ontogeny Underlies Differences in Tumor-Specific Education in Brain Malignancies. Cell Rep. *17*, 2445–2459.

Brastianos, P.K., Carter, S.L., Santagata, S., Cahill, D.P., Taylor-Weiner, A., Jones, R.T., Van Allen, E.M., Lawrence, M.S., Horowitz, P.M., Cibulskis, K., et al. (2015). Genomic Characterization of Brain Metastases Reveals Branched Evolution and Potential Therapeutic Targets. Cancer Discov. *5*, 1164–1177.

Cacalano, G., Lee, J., Kikly, K., Ryan, A.M., Pitts-Meek, S., Hultgren, B., Wood, W.I., and Moore, M.W. (1994). Neutrophil and B cell expansion in mice that lack the murine IL-8 receptor homolog. Science *265*, 682–684.

Chaffer, C.L., San Juan, B.P., Lim, E., and Weinberg, R.A. (2016). EMT, cell plasticity and metastasis. Cancer Metastasis Rev. *35*, 645–654.

Chen, Q., Boire, A., Jin, X., Valiente, M., Er, E.E., Lopez-Soto, A., Jacob, L., Patwa, R., Shah, H., Xu, K., et al. (2016). Carcinoma-astrocyte gap junctions promote brain metastasis by cGAMP transfer. Nature *533*, 493–498.

Choi, H., Sheng, J., Gao, D., Li, F., Durrans, A., Ryu, S., Lee, S.B., Narula, N., Rafii, S., Elemento, O., et al. (2015). Transcriptome analysis of individual stromal cell populations identifies stroma-tumor crosstalk in mouse lung cancer model. Cell Rep. *10*, 1187–1201.

Conway, T., Wazny, J., Bromage, A., Tymms, M., Sooraj, D., Williams, E.D., and Beresford-Smith, B. (2012). Xenome—a tool for classifying reads from xenograft samples. Bioinformatics *28*, i172–i178.

Delattre, J.Y., Krol, G., Thaler, H.T., and Posner, J.B. (1988). Distribution of brain metastases. Arch. Neurol. *45*, 741–744.

Dobin, A., Davis, C.A., Schlesinger, F., Drenkow, J., Zaleski, C., Jha, S., Batut, P., Chaisson, M., and Gingeras, T.R. (2013). STAR: ultrafast universal RNA-seq aligner. Bioinformatics *29*, 15–21.

Doyle, J.P., Dougherty, J.D., Heiman, M., Schmidt, E.F., Stevens, T.R., Ma, G., Bupp, S., Shrestha, P., Shah, R.D., Doughty, M.L., et al. (2008). Application of a translational profiling approach for the comparative analysis of CNS cell types. Cell *135*, 749–762.

Gautier, E.L., Shay, T., Miller, J., Greter, M., Jakubzick, C., Ivanov, S., Helft, J., Chow, A., Elpek, K.G., Gordonov, S., et al.; Immunological Genome Consortium (2012). Gene-expression profiles and transcriptional regulatory pathways that underlie the identity and diversity of mouse tissue macrophages. Nat. Immunol. *13*, 1118–1128.

Goldberg, S.B., Gettinger, S.N., Mahajan, A., Chiang, A.C., Herbst, R.S., Sznol, M., Tsiouris, A.J., Cohen, J., Vortmeyer, A., Jilaveanu, L., et al. (2016). Pembrolizumab for patients with melanoma or non-small-cell lung cancer and untreated brain metastases: early analysis of a non-randomised, open-label, phase 2 trial. Lancet Oncol. *17*, 976–983.

Hanna, A., Boggs, D.H., Kwok, Y., Simard, M., Regine, W.F., and Mehta, M. (2016). What predicts early volumetric edema increase following stereotactic radiosurgery for brain metastases? J. Neurooncol. *127*, 303–311.

Harrell, J.C., Prat, A., Parker, J.S., Fan, C., He, X., Carey, L., Anders, C., Ewend, M., and Perou, C.M. (2012). Genomic analysis identifies unique signatures predictive of brain, lung, and liver relapse. Breast Cancer Res. Treat. *132*, 523–535.

Iuchi, T., Shingyoji, M., Itakura, M., Yokoi, S., Moriya, Y., Tamura, H., Yoshida, Y., Ashinuma, H., Kawasaki, K., Hasegawa, Y., et al. (2015). Frequency of brain metastases in non-small-cell lung cancer, and their association with epidermal growth factor receptor mutations. Int. J. Clin. Oncol. *20*, 674–679.

Jacob, L.S., Vanharanta, S., Obenauf, A.C., Pirun, M., Viale, A., Socci, N.D., and Massagué, J. (2015). Metastatic Competence Can Emerge with Selection of Preexisting Oncogenic Alleles without a Need of New Mutations. Cancer Res. *75*, 3713–3719.

Jiang, C., Xuan, Z., Zhao, F., and Zhang, M.Q. (2007). TRED: a transcriptional regulatory element database, new entries and other development. Nucleic Acids Res. *35*, D137–D140.

Kamar, F.G., and Posner, J.B. (2010). Brain metastases. Semin. Neurol. *30*, 217–235.

Kamp, M.A., Slotty, P.J., Cornelius, J.F., Steiger, H.J., Rapp, M., and Sabel, M. (2018). The impact of cerebral metastases growth pattern on neurosurgical treatment. Neurosurg. Rev. *41*, 77–86.

Kanehisa, M. (2002). The KEGG database. Novartis Found. Symp. *247*, 91–101, discussion 101–103, 119–128, 244–252.

Katic, J., Loers, G., Kleene, R., Karl, N., Schmidt, C., Buck, F., Zmijewski, J.W., Jakovcevski, I., Preissner, K.T., and Schachner, M. (2014). Interaction of the cell adhesion molecule CHL1 with vitronectin, integrins, and the plasminogen activator inhibitor-2 promotes CHL1-induced neurite outgrowth and neuronal migration. J. Neurosci. *34*, 14606–14623.

Khandelwal, G., Girotti, M.R., Smowton, C., Taylor, S., Wirth, C., Dynowski, M., Frese, K.K., Brady, G., Dive, C., Marais, R., and Miller, C. (2017). Next-Generation Sequencing Analysis and Algorithms for PDX and CDX Models. Mol. Cancer Res. *15*, 1012–1016.

Kienast, Y., von Baumgarten, L., Fuhrmann, M., Klinkert, W.E., Goldbrunner, R., Herms, J., and Winkler, F. (2010). Real-time imaging reveals the single steps of brain metastasis formation. Nat. Med. *16*, 116–122.

Kiss, M., Van Gassen, S., Movahedi, K., Saeys, Y., and Laoui, D. (2018). Myeloid cell heterogeneity in cancer: not a single cell alike. Cell. Immunol. *330*, 188–201.

Koch, P.J., and Franke, W.W. (1994). Desmosomal cadherins: another growing multigene family of adhesion molecules. Curr. Opin. Cell Biol. *6*, 682–687.

Koh, H.S., Chang, C.Y., Jeon, S.B., Yoon, H.J., Ahn, Y.H., Kim, H.S., Kim, I.H., Jeon, S.H., Johnson, R.S., and Park, E.J. (2015). The HIF-1/glial TIM-3 axis controls inflammation-associated brain damage under hypoxia. Nat. Commun. *6*, 6340.

Langmead, B., and Salzberg, S.L. (2012). Fast gapped-read alignment with Bowtie 2. Nat. Methods *9*, 357–359.

Lee, H.J., Hanibuchi, M., Kim, S.J., Yu, H., Kim, M.S., He, J., Langley, R.R., Lehembre, F., Regenass, U., and Fidler, I.J. (2016). Treatment of experimental human breast cancer and lung cancer brain metastases in mice by macitentan, a dual antagonist of endothelin receptors, combined with paclitaxel. Neuro-oncol. *18*, 486–496.

Li, Q., and Barres, B.A. (2018). Microglia and macrophages in brain homeostasis and disease. Nat. Rev. Immunol. *18*, 225–242.

Liao, Y., Smyth, G.K., and Shi, W. (2014). featureCounts: an efficient general purpose program for assigning sequence reads to genomic features. Bioinformatics *30*, 923–930.

Lin, Q., Balasubramanian, K., Fan, D., Kim, S.J., Guo, L., Wang, H., Bar-Eli, M., Aldape, K.D., and Fidler, I.J. (2010). Reactive astrocytes protect melanoma cells from chemotherapy by sequestering intracellular calcium through gap junction communication channels. Neoplasia *12*, 748–754.

Love, M.I., Huber, W., and Anders, S. (2014). Moderated estimation of fold change and dispersion for RNA-seq data with DESeq2. Genome Biol. *15*, 550.

Ludwig, H.C., Ahkavan-Shigari, R., Rausch, S., Schallock, K., Quentin, C., Ziegler, D., Bockermann, V., and Markakis, E. (2000). Oedema extension in cerebral metastasis and correlation with the expression of nitric oxide synthase isozymes (NOS I-III). Anticancer Res. *20*, 305–310.

Maness, P.F., and Schachner, M. (2007). Neural recognition molecules of the immunoglobulin superfamily: signaling transducers of axon guidance and neuronal migration. Nat. Neurosci. *10*, 19–26.

Mao, X., Ou, M.T., Karuppagounder, S.S., Kam, T.I., Yin, X., Xiong, Y., Ge, P., Umanah, G.E., Brahmachari, S., Shin, J.H., et al. (2016). Pathological α-synuclein transmission initiated by binding lymphocyte-activation gene 3. Science *353*, aah3374.

Minn, A.J., Kang, Y., Serganova, I., Gupta, G.P., Giri, D.D., Doubrovin, M., Ponomarev, V., Gerald, W.L., Blasberg, R., and Massagué, J. (2005). Distinct organ-specific metastatic potential of individual breast cancer cells and primary tumors. J. Clin. Invest. *115*, 44–55.

Nguyen, D.X., Chiang, A.C., Zhang, X.H., Kim, J.Y., Kris, M.G., Ladanyi, M., Gerald, W.L., and Massagué, J. (2009). WNT/TCF signaling through LEF1 and HOXB9 mediates lung adenocarcinoma metastasis. Cell *138*, 51–62.

Park, E.S., Kim, S.J., Kim, S.W., Yoon, S.L., Leem, S.H., Kim, S.B., Kim, S.M., Park, Y.Y., Cheong, J.H., Woo, H.G., et al. (2011). Cross-species hybridization of microarrays for studying tumor transcriptome of brain metastasis. Proc. Natl. Acad. Sci. USA *108*, 17456–17461.

Pekny, M., and Nilsson, M. (2005). Astrocyte activation and reactive gliosis. Glia *50*, 427–434.

Priego, N., Zhu, L., Monteiro, C., Mulders, M., Wasilewski, D., Bindeman, W., Doglio, L., Martínez, L., Martínez-Saez, E., Ramón y Cajal, S., et al. (2018). STAT3 labels a subpopulation of reactive astrocytes required for brain metastasis. Nat. Med. *24*, 1024–1035.

Sato, R., Nakano, T., Hosonaga, M., Sampetrean, O., Harigai, R., Sasaki, T., Koya, I., Okano, H., Kudoh, J., Saya, H., and Arima, Y. (2017). RNA Sequencing Analysis Reveals Interactions between Breast Cancer or Melanoma Cells and the Tissue Microenvironment during Brain Metastasis. BioMed Res. Int. *2017*, 8032910.

Schleusener, J.T., Tazelaar, H.D., Jung, S.H., Cha, S.S., Cera, P.J., Myers, J.L., Creagan, E.T., Goldberg, R.M., and Marschke, R.F., Jr. (1996). Neuroendocrine differentiation is an independent prognostic factor in chemotherapy-treated nonsmall cell lung carcinoma. Cancer *77*, 1284–1291.

Sevenich, L., Bowman, R.L., Mason, S.D., Quail, D.F., Rapaport, F., Elie, B.T., Brogi, E., Brastianos, P.K., Hahn, W.C., Holsinger, L.J., et al. (2014). Analysis of tumour- and stroma-supplied proteolytic networks reveals a brain-metastasis-promoting role for cathepsin S. Nat. Cell Biol. *16*, 876–888.

Shannon, P., Markiel, A., Ozier, O., Baliga, N.S., Wang, J.T., Ramage, D., Amin, N., Schwikowski, B., and Ideker, T. (2003). Cytoscape: a software environment for integrated models of biomolecular interaction networks. Genome Res. *13*, 2498–2504.

Stevens, L.E., Cheung, W.K.C., Adua, S.J., Arnal-Estapé, A., Zhao, M., Liu, Z., Brewer, K., Herbst, R.S., and Nguyen, D.X. (2017). Extracellular Matrix

Receptor Expression in Subtypes of Lung Adenocarcinoma Potentiates Outgrowth of Micrometastases. Cancer Res. *77*, 1905–1917.

Stillie, R., Farooq, S.M., Gordon, J.R., and Stadnyk, A.W. (2009). The functional significance behind expressing two IL-8 receptor types on PMN. J. Leukoc. Biol. *86*, 529–543.

Strand, A.D., Aragaki, A.K., Baquet, Z.C., Hodges, A., Cunningham, P., Holmans, P., Jones, K.R., Jones, L., Kooperberg, C., and Olson, J.M. (2007). Conservation of regional gene expression in mouse and human brain. PLoS Genet. *3*, e59.

Streit, W.J., Braak, H., Xue, Q.S., and Bechmann, I. (2009). Dystrophic (senescent) rather than activated microglial cells are associated with tau pathology and likely precede neurodegeneration in Alzheimer's disease. Acta Neuropathol. *118*, 475–485.

Stummer, W. (2007). Mechanisms of tumor-related brain edema. Neurosurg. Focus *22*, E8.

Su, H., Xie, H., Dai, C., Ren, Y., She, Y., Xu, L., Chen, D., Xie, D., Zhang, L., Jiang, G., and Chen, C. (2018). Characterization of TIM-3 expression and its prognostic value in patients with surgically resected lung adenocarcinoma. Lung Cancer *121*, 18–24.

Subramanian, A., Tamayo, P., Mootha, V.K., Mukherjee, S., Ebert, B.L., Gillette, M.A., Paulovich, A., Pomeroy, S.L., Golub, T.R., Lander, E.S., and Mesirov, J.P. (2005). Gene set enrichment analysis: a knowledge-based approach for interpreting genome-wide expression profiles. Proc. Natl. Acad. Sci. USA *102*, 15545–15550.

Takei, H., Rouah, E., and Ishida, Y. (2016). Brain metastasis: clinical characteristics, pathological findings and molecular subtyping for therapeutic implications. Brain Tumor Pathol. *33*, 1–12.

Therneau, T.M., and Grambsch, P.M. (2000). Modeling Survival Data: Extending the Cox Model (Springer).

Uhlén, M., Fagerberg, L., Hallström, B.M., Lindskog, C., Oksvold, P., Mardinoglu, A., Sivertsson, Å., Kampf, C., Sjöstedt, E., Asplund, A., et al. (2015). Proteomics. Tissue-based map of the human proteome. Science *347*, 1260419.

Urday, S., Kimberly, W.T., Beslow, L.A., Vortmeyer, A.O., Selim, M.H., Rosand, J., Simard, J.M., and Sheth, K.N. (2015). Targeting secondary injury in intracerebral haemorrhage—perihaematomal oedema. Nat. Rev. Neurol. *11*, 111–122.

Valiente, M., Obenauf, A.C., Jin, X., Chen, Q., Zhang, X.H., Lee, D.J., Chaft, J.E., Kris, M.G., Huse, J.T., Brogi, E., and Massagué, J. (2014). Serpins promote cancer cell survival and vascular co-option in brain metastasis. Cell *156*, 1002–1016.

Valiente, M., Ahluwalia, M.S., Boire, A., Brastianos, P.K., Goldberg, S.B., Lee, E.Q., Le Rhun, E., Preusser, M., Winkler, F., and Soffietti, R. (2018). The Evolving Landscape of Brain Metastasis. Trends Cancer *4*, 176–196.

Wang, Y., Klijn, J.G., Zhang, Y., Sieuwerts, A.M., Look, M.P., Yang, F., Talantov, D., Timmermans, M., Meijer-van Gelder, M.E., Yu, J., et al. (2005). Gene-expression profiles to predict distant metastasis of lymph-node-negative primary breast cancer. Lancet *365*, 671–679.

Weledji, E.P., and Assob, J.C. (2014). The ubiquitous neural cell adhesion molecule (N-CAM). Ann. Med. Surg. (Lond) *3*, 77–81.

Wiener, Z., Kohalmi, B., Pocza, P., Jeager, J., Tolgyesi, G., Toth, S., Gorbe, E., Papp, Z., and Falus, A. (2007). TIM-3 is expressed in melanoma cells and is upregulated in TGF-beta stimulated mast cells. J. Invest. Dermatol. *127*, 906–914.

Williams, A.F., and Barclay, A.N. (1988). The immunoglobulin superfamily—domains for cell surface recognition. Annu. Rev. Immunol. *6*, 381–405.

Winslow, M.M., Dayton, T.L., Verhaak, R.G., Kim-Kiselak, C., Snyder, E.L., Feldser, D.M., Hubbard, D.D., DuPage, M.J., Whittaker, C.A., Hoersch, S., et al. (2011). Suppression of lung adenocarcinoma progression by Nkx2-1. Nature *473*, 101–104.

Xie, T.X., Huang, F.J., Aldape, K.D., Kang, S.H., Liu, M., Gershenwald, J.E., Xie, K., Sawaya, R., and Huang, S. (2006). Activation of stat3 in human melanoma promotes brain metastasis. Cancer Res. *66*, 3188–3196.

Xu, C., Wang, T., Cheng, S., and Liu, Y. (2013). Increased expression of T cell immunoglobulin and mucin domain 3 aggravates brain inflammation via regulation of the function of microglia/macrophages after intracerebral hemorrhage in mice. J. Neuroinflammation *10*, 141.

Yuan, X., Li, Z., Baines, A.C., Gavriilaki, E., Ye, Z., Wen, Z., Braunstein, E.M., Biesecker, L.G., Cheng, L., Dong, X., and Brodsky, R.A. (2017). A hypomorphic PIGA gene mutation causes severe defects in neuron development and susceptibility to complement-mediated toxicity in a human iPSC model. PLoS ONE *12*, e0174074.

Zhang, X.H., Jin, X., Malladi, S., Zou, Y., Wen, Y.H., Brogi, E., Smid, M., Foekens, J.A., and Massagué, J. (2013). Selection of bone metastasis seeds by mesenchymal signals in the primary tumor stroma. Cell *154*, 1060–1073.

Zhang, Y., Chen, K., Sloan, S.A., Bennett, M.L., Scholze, A.R., O'Keeffe, S., Phatnani, H.P., Guarnieri, P., Caneda, C., Ruderisch, N., et al. (2014). An RNA-sequencing transcriptome and splicing database of glia, neurons, and vascular cells of the cerebral cortex. J. Neurosci. *34*, 11929–11947.

Zhang, H., Xiang, R., Wu, B., Li, J., and Luo, G. (2017). T-cell immunoglobulin mucin-3 expression in invasive ductal breast carcinoma: Clinicopathological correlations and association with tumor infiltration by cytotoxic lymphocytes. Mol. Clin. Oncol. *7*, 557–563.

Zhu, C., Anderson, A.C., Schubart, A., Xiong, H., Imitola, J., Khoury, S.J., Zheng, X.X., Strom, T.B., and Kuchroo, V.K. (2005). The Tim-3 ligand galectin-9 negatively regulates T helper type 1 immunity. Nat. Immunol. *6*, 1245–1252.

Zhuang, X., Zhang, X., Xia, X., Zhang, C., Liang, X., Gao, L., Zhang, X., and Ma, C. (2012). Ectopic expression of TIM-3 in lung cancers: a potential independent prognostic factor for patients with NSCLC. Am. J. Clin. Pathol. *137*, 978–985.

STAR★METHODS

KEY RESOURCES TABLE

REAGENT or RESOURCE	SOURCE	IDENTIFIER
Antibodies		
Rabbit monoclonal, Anti-TMEM119 1:250, Stock: 0.1 mg/ml, (Clone 28-3) Lot# GR3207309-2	abcam	Cat#ab209064; RRID: AB_2728083
Mouse monoclonal Anti-LAG3, 1:250, Stock: 1mg/ml, (Clone 4-10-C9) Lot# 2943580	Millipore	Cat#MABF954; N/A
Rabbit monoclonal Anti- LAG3, 1:250, Stock: 0.981 mg/ml (Clone EPR20294-77), Lot# GR3203111-1	Abcam	Cat #ab209238; N/A
Goat Polyclonal Anti-IBA1, 1:500, Stock: 0.5mg/ml, Lot# S9G2P2E060818	NovusBio	Cat#NB100-1028; RRID:AB_521594
Rabbit Polyclonal Anti-IBA1, 1:500, Lot# PTN5930	Wako Pure Chemical Industries	Cat#019-19741; RRID:AB_839504
Chicken Polyclonal Anti-GFP, 1:500, Stock: 10mg/ml, Lot# GR3190550-8	abcam	Cat#ab13970; RRID:AB_300798
Goat polyclonal anti-Vimentin, 1:10, Lot# ADRK0113051	R&D Systems	Cat#IC8104G; N/A
Rabbit Polyclonal anti-GFAP, 1:500, Lot# 2812020	Millipore	Cat#AB5804; RRID:AB_2109645
Mouse Monoclonal Anti-LY6G, 1:100, Stock: 0.2mg/ml, (Clone: 1A8) Lot# B184949	Biolegend	Cat#127613; RRID:AB_1877163
Mouse Monoclonal Pan-Cytokeratin, 1:100, Stock: 0.5 mg/ml, (Clone: AE1/AE3) Lot# 1998204	Thermo Scientific	Cat#53-9003-80; RRID: AB_1834351
Rabbit Polyclonal Anti-NeuN, 1:500, Lot# 2972808	Millipore	Cat#ABN78; RRID: AB_10807945
Rabbit Polyclonal Anti-TIM3, 1:250, Stock: 1.32 mg/ml, Lot# GR3191882-7, (HUMAN Staining)	Abcam	Cat#ab185703; N/A
Goat Polyclonal Anti-TIM3, 1:250, Stock: 0.2 mg/ml, Lot: IXQ0216121 (Mouse Staining)	R&D Systems	Cat#AF1529; RRID: AB_354845
Mouse Monoclonal Anti-Melanoma gp100, 1:100 (Clone: HMB45)	Abcam	Cat#ab787; RRID: AB306146
Rabbit Monoclonal Anti-TIM3 1:250, Stock: 16 ug/ml, Lot#: 1, (Clone: D5D5R) (HUMAN Staining)	Cell Signaling	Cat#45208; RRID:AB_2716862
Biological Samples		
Human Brain Metastatic Melanoma	Yale University Protocol#: 2000021359	VC004
Human Brain Metastatic Sacromatoid Carcinoma	Yale University Protocol#: 2000021359	BMTP6
Human Brain Metastatic Patient-Derived Xenografts	Yale University (Protocol#: 1110009228 and 1603017333)	YUL0063 and YLR076
Critical Commercial Assays		
QIAzol Lysis Reagent	QIAGEN	Cat#79306
QIAshredder	QIAGEN	Cat#79656
RNeasy Lipid Tissue mini kit	QIAGEN	Cat#74804
Taqman Universal PCR Master Mix	Applied Biosystems	Cat#4324018
Deposited Data		
Expression data from primary breast tumors	Bos et al., 2009	EMC192 (GSE12276)
Expression data from primary breast tumors	Wang et al., 2005	EMC286 (GSE2034)
Expression data from primary breast tumors	Minn et al., 2005	MSK82 (GSE2603)
Expression data from primary breast tumors	Harrell et al., 2012	NKI295

(*Continued on next page*)

Continued

REAGENT or RESOURCE	SOURCE	IDENTIFIER
BMX-Sequencing raw data	This Paper	GSE115699, GSE115700, GSE115701, (GSE115702 = reference series)
Analysis Pipeline	This Paper	https://github.com/zz2liu/bmx_seq
Experimental Models: Cell Lines		
Human: H2030-BrM3	Memorial Sloan Kettering	Passaged through the brain three times (Nguyen et al., 2009)
Human: MDA231-BrM2	Memorial Sloan Kettering	Passaged through the brain two times (Bos et al., 2009)
Human: A375-Br	Laboratory of Dr. Suyen Huang (MD Anderson)	Passaged through the brain three times (Xie et al., 2006)
Mouse: 368T1	Laboratory of Dr. Monte Winslow (Stanford)	Passaged through the brain one time (This paper). (Winslow et al., 2011)
Experimental Models: Organisms/Strains		
B6129SF1/J *Mus musculus*	Jackson Lab	Cat#101043; RRID:IMSR_JAX:101043
Athymic Nude-Foxn1^{nu} (nu/nu) *Mus musculus*	Charles River	Cat#088; RRID:IMSR_CRL:088
NOD.Cg-Prkdc^{scid} Il2rg^{tm1Wjl}/SzJ *Mus musculus*	Jackson Lab	Cat# 05557; RRID:IMSR_JAX005557
Oligonucleotides		
Oligonucleotides	Table S7	N/A
Software and Algorithms		
ImageJ 1.51f	National Institutes of Health	RRID:SCR_003070 https://imageJ.nih.gov/ij
Trim Galore	Barbraham Bioinfromatics Krueger., 2015	https://www.bioinformatics.babraham.ac.uk/projects/trim_galore/
Bowtie2	Langmead and Salzberg, 2012	http://bowtie-bio.sourceforge.net/bowtie2/index.shtml
Xenome	Conway et al., 2012	https://github.com/data61/gossamer
ConBowtie	This Paper	Aligned to concatenated genome with Bowtie2, count to human and mouse transcriptomes separately to get count matrices.
STAR	Dobin et al., 2013	https://github.com/alexdobin/STAR
featureCounts	Liao et al., 2014	http://subread.sourceforge.net/
DESeq2 R Package	Love et al., 2014	https://bioconductor.org/packages/release/bioc/html/DESeq.html
Gene Set Enrichment Analysis (GSEA)	Subramanian et al., 2005	http://software.broadinstitute.org/gsea/index.jsp
Prism Version 7.0a		https://www.graphpad.com/scientific-software/prism/
Metacore	Clarivate Analytics	https://portal.genego.com/
The Human Protein Atlas (v18)	Uhlén et al., 2015	https://www.proteinatlas.org
Partek 7.18.0518		http://www.partek.com/
Survival R Package	Therneau., 2000	https://cran.r-project.org/web/packages/survival/index.html
Survminor R Package		https://cran.r-project.org/web/packages/survminer/index.html
Other		
Resource Website	This Paper	http://bmxexplorer.gotdns.org/

CONTACT FOR REAGENT AND RESOURCE SHARING

Further information and requests for resources and reagents should be directed to and will be fulfilled by the Lead Contact, Don Nguyen (don.nguyen@yale.edu).

EXPERIMENTAL MODEL AND SUBJECT DETAILS

Primary Cell Culture

Human cell lines H2030-BrM3 (male), MDA-MB-231 BrM2 (female), and A375-Br (female) were generated following 2-3 cycles of *in vivo* selection following intra-arterial injection and brain colonization (Bos et al., 2009; Nguyen et al., 2009; Xie et al., 2006). Prior to selection, metastatic or parental cells were infected with a lentivirus encoding for a thymidine kinase, GFP, and luciferase reporter gene (Minn et al., 2005; Nguyen et al., 2009). H2030-BrM3, MDA231-BrM2, and A375-Br brain metastatic cells were cultured under the same conditions as their parental lines and as recommended by the American Type Culture Collection with 10% Fetal Bovine Serum (FBS), 1% penicillin-streptomycin and 0.2% amphotericin B (including prior to RNA extraction). Cell line identification was confirmed 2 weeks prior to injection into mice using STR analysis by the Yale Cell Line Authentication Service. For monolayer cultures, cells were passaged every 3-4 days and cultured unperturbed for at least three days before harvesting at 70%–80% confluence. 368T1-Br cells were derived from the brain of syngeneic mice following 1 round of intra-arterial injection of the parental 368T1 cell line and were maintained in DME media supplemented with 10% fetal bovine serum (FBS), 2 mM L-Glutamine, 100IU/ml penicillin/streptomycin and 1 μg/ml amphotericin (Winslow et al., 2011).

Mice

For human cell line xenografts, 4-5 week old athymic nu/nu mice were purchased from Charles River (strain code 088). For injection of 368T1-Br syngeneic model, 4-5 week old, male, B6129SF1/J mice (Jackson Lab) were used. For PDX YUL0063 described below, male, NSG mice were used (Jackson Lab, Cat #: 005557). All mice were allowed to acclimate for one week at our animal facility after their arrival date before experiments were initiated. Mice were housed in sex-matched groups (n = 4-5 mice per cage) with food and water available *ad libitum*. All animal studies were approved by the Yale University Institutional Animal Care and Use Committee (IACUC). Tumor growth was monitored by bioluminescent imaging using an IVIS Spectrum. The influence of sex was not explicitly analyzed in this study because the sex of each animal was matched to that of the cell line or PDX that was injected, with the exception being for experiments where the H2030-BrM3, MDA231-BrM2, and A375-BrM models were directly compared to one another and all injected into male athymic mice (Figure S7A).

Patient Derived Xenografts

Patients with advanced lung cancer who developed acquired resistance to approved or experimental targeted agents or immunotherapies provided consent and were enrolled to a Yale University Institutional Review Board–approved protocols (#1110009228, #1603017333), in accordance with ethical guidelines, allowing the collection and analysis of clinical data, archival, fresh tissue, and the generation of PDXs. YLR076 was resected from the left cerebellar region of a male patient, age 67 and YUL0063 was resected from the left cerebellar region of a female patient, age 63. Both biopsies were first transplanted and maintained as subcutaneous tumors. Driver mutation *(KRAS)* for YUL0063 was validated using Sanger sequencing prior to injection. YLR076 was validated by exome sequencing prior to cell line generation and has unknown driver mutation status. A pathologist confirmed the histology (YLR076 = squamous cell carcinoma; YUL0063 = neuroendocrine carcinoma) of biopsies, and their matched subcutaneous and brain orthotopic PDXs (YLR076 at passage 5, YUL0063 at passage 1). A cell line of YLR076 was dissociated from a subcutaneous PDX at passage 5 using an enzymatic cocktail of Collagenase IV (2mg/ml), Hyaluronidase (0.5mg/ml), Dispase (3mg/ml) and DNase (1ug/ml) in HBSS. YLR076 cells were infected with a lentivirus encoding reporter gene (Minn et al., 2005) before intra-cranial injection into the murine brain. YUL0063 was dissociated from a subcutaneous PDX (passage 4) using the enzymatic cocktail described above and injected subcutaneously into the murine flank or intra-cranially into the murine brain. Both PDXs were tested for *Mycoplasma* and murine viral contamination by the Yale University Molecular Diagnostics Laboratory prior to the experiments reported here. For mRNA analysis of YUL0063 FBMet and s.c. samples, 4 s.c. tumors and 4 FBMet tumors were analyzed. For mRNA analysis of YLR076, 5 FBMet tumors were analyzed and 3 samples harvested in monolayer. One tumor was analyzed per mouse and tumor samples across mice were compared. Take rates for YUL0063 post-injection were 100% (4/4) for subcutaneous tumors and 83% (15/18) for FBMet tumors post intra-cranial injections. Take rates for YLR076 were 87% (13/15) for FBMet tumors post intra-cranial injections.

Additional Human Tissue

Patients with brain metastasis provided informed consent and were enrolled to a Yale University Institutional Review Board–approved protocol #2000021359, in accordance with ethical guidelines, allowing the collection and analysis of clinical data, archival, fresh tissue, and the generation of patient derived cell cultures and PDXs. Brain metastasis tissue BMTP6 was resected from the frontal lobe of a female patient, age 56, with metastatic melanoma. Tumor was positive for HMB45. Brain metastasis tissue VC004 was resected from the occipital lobe of a male patient, age 74, with NSCLC (sarcomatoid carcinoma). Tumor was positive for pan-cytokeratin.

METHOD DETAILS

Intra-arterial Injections

For the human cell xenograft H2030-BrM3 FBMet-HBMet-s.c.-2D comparison, $5x10^5$ cells in 100 ul PBS were injected into the left-ventricle of 5-6 week old athymic nu/nu mice. Sham injected mice were injected intra-arterially with PBS alone. Tumors were collected at 21 days post inoculation as determined by tumor burden. One forebrain metastatic tumor (FBMet) and one hindbrain metastatic tumor (HBMet) were collected per animal (Figure S2C) and tumors from independent mice were compared. For the human cell xenograft H2030-BrM3 FBMet-LuOt comparison, $1x10^5$ cells were injected intra-arterially as described above and tumors were collected at 42-49 days. Again, as above, one FBMet tumor was collected per animal.

Intra-cranial Injections

For the H2030-BrM3, MDA231-BrM2, and A375-BrM models, $1x10^5$, $1x10^4$ and $1x10^5$ cells respectively were injected intra-cranially in 1 ul of FBS into 5-6 week old athymic nu/nu mice. For the 368T1-Br syngeneic model, 5-6 week old B6129SF1/J mice were injected with $5x10^2$ cells intra-cranially. For PDX YLR076 and YUL0063, $1x10^5$ and $2x10^5$ cells were injected into athymic nu/nu mice and NSG mice, respectively. All intra-cranial injections were accomplished using a digital mouse stereotactic instrument (Braintree Scientific; 51725-D) and sham injected mice were injected with 1 ul of FBS alone. The injection site was 2 mm lateral from the bregma. Tumors were grown for 14-21 days, except for YUL0063 (48 days). One forebrain metastatic tumor (FBMet) was collected per animal (Figure S6A).

Subcutaneous Injections

Human cell xenograft subcutaneous injections were accomplished using $5x10^5$ cells in 100ul PBS mixed with 50% growth factor reduced matrigel (Fisher Scientific; 356231) before injection into the flank of 5-6 week old athymic nu/nu mice. For PDX YUL0063, $2x10^5$ cells were injected. Subcutaneous tumors were measured weekly and tissue was harvested when tumor volume reached 100-200 mm^3 (14-25 days). One subcutaneous tumor was collected per animal.

Orthotopic Injections

For orthotopic lung tumors $2x10^4$ H2030-BrM3 cells were injected intratracheally. To do this, a small 0.5 cm incision was performed on the skin covering the right part of the lateral thorax to expose the thoracic wall. An insulin needle was inserted 3 mm deep into the 4^{th} intercostal space when the lung could be visualized through the thoracic wall. A mixture of $2x10^4$ H2030-BrM3 cells were diluted 1:1 in Matrigel (total volume = 100 μl) and then injected. After injection, the needle was held for 30 s within the injection site and then removed. The skin was closed with several stitches. 21 days post inoculation, lung tumors were macrodisssected as described in *RNA Collection for BMX-Seq analysis*. One LuOt tumor was collected per animal.

RNA Collection for BMX-Seq Analysis

To determine the location of brain metastatic tumors, murine brains were extracted from the skull and imaged *ex vivo* by bioluminescent imaging. Tumor or healthy tissue was macrodissected with a scalpel and immediately flash frozen in liquid nitrogen. The total tissue collected included surrounding stromal regions. FB and HB control regions originated from sham-injected mice and were macrodissected from the same corresponding brain regions as FBMet and HBMet samples. FBMet and FB samples included the area approximately anterior to the lateral ventricles. HBMet and HB samples included predominantly the cerebellum (Figure S2C). Post intra-arterial injection, FBMet and HBMet paired samples were collected from independent mice (n = 3 mice; total samples = 6.), as were FBMet samples collected post intra-cranial injection (n = 2-3). Similarly, healthy FB (n = 3-5), healthy HB (n = 4), subcutaneous tumors (n = 4) and lung tumors (n = 2) were collected from independent mice. Samples harvested in monolayer were harvested at 70%–80% confluency (n = 3). Cell lysates were homogenized using QIAzol Lysis Reagent (QIAGEN; 79306) and a cell scraper where applicable (Corning; 353085), before being spun down in QIAshredder tubes (QIAGEN; 79656). Samples harvested *in vivo* and *in vitro* were extracted in parallel using the RNeasy Lipid Tissue mini kit (QIAGEN; 74804). Samples were sequenced on a HiSeq 2500 (Illumina) with paired-end 75 base pair reads. The BMX-seq pipeline is described in full under *BMX-Seq Analysis and Pipeline* below.

BMX-Seq Analysis and Pipeline

As depicted in Figure S1, we compared the ability of three pipelines to align RNA seq reads to either the human (tumor) or mouse (stroma) genome and transcriptome. For the Xenome pipeline, reads trimmed of adaptor sequences (Trim Galore: Barbraham Bioinformatics, Felix Krueger) were first classified with Xenome (Conway et al., 2012). Reads that classified as graft were aligned to the human genome and transcriptome and those that classified as host were aligned to the mouse genome and transcriptome using STAR (Dobin et al., 2013). For the ConBowtie and BMX-Seq pipelines, a combined genome was constructed using human (hg38) and mouse (mm10) genomes. Reads uniquely aligned to the combined genome were then extracted to separate bam files, one for human and one for mouse. Using the ConBowtie method, bowtie2–local mode was used to allow junction reads to be mapped

to one of the exons independent of gene annotations (Langmead and Salzberg, 2012). Using the BMX-seq method, reads were trimmed of adaptor sequences and then mapped to the combined genome and combined gene annotation (GENCODE v24 for human, vM10 for mouse) using STAR.

To calculate differential gene expression, the uniquely mapped reads (MAPQ > = 10) were counted to gene annotations using featureCounts (Liao et al., 2014), thus generating a count matrix of gene by sample. The matrix was then used as input to DESeq2 R package (Love et al., 2014). To exclude mouse reads inaccurately mapping to the human genome and human reads inaccurately mapping to the mouse genome, the cross-mapping rate for a specific gene from all reads mapped to the opposite genome (mouse or human) was determined. Mouse only (sham-injected) and human only (tumor cells grown in monolayer) samples were used as normalizing controls to estimate the cross-mapping rate to a human or mouse gene. If the predicted cross-mapping reads that mapped to a particular gene exceeded 10% of the total reads mapped to that gene, then the gene was excluded from our final curated gene lists. These genes are annotated in a downloadable table on our web portal (http://bmxexplorer.gotdns.org/).

To evaluate the mapping performance, reads from sham injected mice were aligned to the mouse genome using bowtie2–local. Uniquely mapped reads were then used as a standard of mouse reads. A subset of one million of such accurate reads were randomly picked as a test set. Similarly, reads from tumor cells grown in monolayer were processed and used as a standard of human reads.

Isolation and Re-plating of Brain Metastatic Cells

After 18 to 21 days post intra-arterial injection of H2030-BrM3 cells, tumor lesions were macrodissected and collected in 2% penicillin streptomycin, 0.04% amphotericin B solution in PBS. Tissues were then minced and incubated at 37° for one hour in 2% penicillin streptomycin, 0.04% amphotericin B, 0.125% collagenase III, and 0.1% hyaluronidase in RPMI media. Samples were vortexed every 10 minutes. Post incubation, samples were spun down and suspended in 2% penicillin streptomycin, 0.04% amphotericin B solution in 0.25 Trypsin for 20 minutes at 37°. Samples were then washed in 2% penicillin streptomycin, 0.04% amphotericin B solution in PBS for two rounds before being plated in 6 cm tissue culture treated dishes. Cells were harvested at 70%–80% confluence for 3 passage cycles.

Varying Confluence in Monolayer

To seed H2030-BrM3 cells at varying density, $2x10^5$ (80%), $1x10^5$ (60%), $7x10^4$ (40%), and $3x10^4$ (10%) cells were seeded in a 6-well dish (Costar; 3516). Cells were allowed to grow for 4 days with one media change on day 2. On day 4, cells were harvested for RNA using the method described in *RNA Collection for BMX-Seq Analysis.*

Species Specific qRT-PCR

RNA was measured by a Nanodrop spectrophotometer. 1 ug of mRNA was reverse transcribed into cDNA using iScript cDNA Synthesis Kit (Bio-Rad; P1708891). PCR of cDNA was completed using TaqMan Universal Master Mix no AmpErase UNG (Applied Biosystems; 4324018). Species-specific TaqMan primers (20x) were designed and ordered through Applied Biosystems. qRT-PCR reactions were run in quadruplicate and data was normalized to housekeeping genes *HPRT1* (human), *ACTB* (human) or *Hprt* (mouse). All Taqman primers were run in mouse only and human only samples to confirm preferential cDNA amplification of the target gene of interest in the proper compartment (tumor or stroma). All qPCRs are shown as the mean fold change across indicated samples ± SEM. All TaqMan primer sequences used are listed in Table S7.

Murine Immunofluorescent Staining and Image Acquisition

Mice were anesthetized and sacrificed, followed by perfusion with 5 mL of PBS through the left ventricle. Tissue was fixed overnight in 4% PFA at 4°C, washed 3 times in 0.2 M sodium phosphate solution and embedded in 2% LE agarose. Tissue was sectioned (50 μm) using a Vibrotome (Campden Instruments; Model 5100mz) and stored in cryostorage solution (1% PVP40 (Sigma; 9003-39-8), 30% sucrose, 30% ethylene glycol in 0.2 M sodium phosphate). On the day of IF staining, tissues were washed in PBS for 15 minutes. IF experiments, except those including anti-mTIM3 antibody (R&D Systems; AF1529), were blocked in 0.1% Triton X-100 (American Bioanalytical; AB02025) and 0.3% bovine serum albumin (BSA) (Sigma; A9647) in PBS for 1 hour before incubation overnight in primary antibody (4°C). Sections were then washed in PBS for 15 minutes and incubated for 1 hour at room temperature in 0.1% Triton X-100 and 0.3% BSA in PBS with fluorescent secondary antibody. Sections were washed in PBS for 15 minutes and then mounted on slides using prolong gold antifade reagent (Cell Signaling Technology; 9071). All IF staining requiring the antibody anti-mTIM3 were similarly washed and then blocked in a 0.1% Triton X-100, 10% donkey serum (Sigma Aldrich; D9663) solution in PBS for 1 hour. Primary antibody incubation and washing steps were accomplished as described above and secondary antibody incubated for 2 hours. All IF images were obtained using a Keyence microscope (BZ-X700) at 4x,10x, 20x or 40x magnification. 40x and 20x images are z stack projections and all image processing (stacking, brightness, contrast) was done using the Keyence or ImageJ software. Images that are directly compared were stained at the same time, imaged with the same exposure time for each relative channel and processed in parallel.

Human Immunofluorescent Staining

Human brain metastatic tissues were collected and placed in 10% formalin overnight before embedding in paraffin. 5 μm paraffin sections were heated at 65°C for 25 minutes followed by two 10 minute washes in xylene and two 10 minute washes in ethanol. Following ethanol washes, sections were gradually diluted with H2O (20 minutes). 1.21 g of Tris hydroxymethyl aminomethane and 0.37 g of EDTA were dissolved in 1000 mL of distilled water, with 500 μL of Tween-20 (Sigma; P7949) and heated to 99°C (pH = 9.25). Sections were added to heated solution and incubated for 20 minutes. Following antigen retrieval, sections were washed in H2O three times, TBST three times and then blocked for 1 hour with 5% donkey serum (Sigma Aldrich; D9663) and 0.1% Triton X-100 (American Bioanalytical; AB02025). Primary antibodies were incubated overnight at 4° in 0.3% donkey serum and 0.1% Triton X-100. Tissue was washed for 15 minutes in TBST and secondary antibodies were incubated in the same solution as the primary incubation for one hour at room temperature the following day. Sections were then washed in TBST for 15 minutes and mounted on slides using prolong gold antifade reagent (Cell Signaling Technology; 9071).

Tumor-Stroma Crosstalk Network Analysis

CCCExplorer (Choi et al., 2015) was utilized to identify the paracrine crosstalk network predicted by the data from the BMX-seq pipeline. From annotated ligand-receptor pairs, we identified ligands upregulated in the forebrain metastatic stroma as compared to the s.c. stroma and receptors from corresponding pathways that are expressed in tumor cells (LR_u) grown in the brain. From transcription factor (TF)-target pairs annotated in KEGG (Kanehisa, 2002) and TRED (Jiang et al., 2007), we identified TFs that were 1) expressed in tumor cells and 2) showed significantly upregulated expression of corresponding downstream targets (TF_a) in FBMet samples as compared to s.c. tumor samples. For each annotated pathway with at least one LR_u and one TF_a, we generated a subgraph from the LR_us and TF_as with intermediate connecting nodes and labeled these as activated if the target genes from the TF_as were significantly enriched. Each activated subgraph is extended with activated targeting genes and visualized as in Shannon et al. (Shannon et al., 2003). All genes were included in this analysis with the following thresholds: RPKM > 2 for gene expressed, FDR < 0.05 for genes upregulated.

Gene Set Enrichment, Pathway Analysis and Heatmap Generation

Metacore from Clarivate Analytics (https://portal.genego.com/) analysis was conducted using gene lists filtered by significance (adjusted p value of < 0.05) for each experimental comparison in question. Enrichment Analysis was performed. Plotted are pathway maps and process networks with the most significant *p-value*s. Neuroendocrine Tumors enrichment score was plotted from the grouping Diseases (by Biomarkers). Enrichment scores were calculated based on $-\log_{10}$ (p value) with p value determined by Metacore. Gene Set Enrichment Analysis (Subramanian et al., 2005) was conducted using rank gene lists. Rank gene lists were generated based on the direction of fold change multiplied by the inverse adjusted p value of the comparison in question for each transcript annotated. Enrichment statistic: classic. Gene sets listed below were determined as significantly enriched after ranked gene lists were run against the GO gene set collection c5.bp.v6.1. Rank of each listed gene set was determined by the significance of pathway enrichment as compared to other pathways in the GO gene set c5.bp.v6.1. Ie. "1" indicates this was the top pathway enriched in the given comparison. Genes considered to be differentially expressed across our own datasets are those that have an adjusted p value < 0.05 for the comparisons in question. PCA plots, hierarchical clustering (Pearson's Dissimilarity), and heatmaps were generated in R and Partek. Genes with an average RPKM < 1.0 across samples (in a given comparison), lincRNAs and pseudogenes were excluded from heatmaps.

GSEA Gene Sets

GO_Cell_Projection_Assembly,	M10772
GO_Regulation of Neuron Differentiation,	M12739
GO_Neuron_Projection_Guidance,	M15608
GO_Chromatin_Modification,	M12761
GO_Cell_Morphogenesis_Involved_In_Differentiation,	M13801
GO_Cell_Morphogenesis_Involved_In_Neuron_Differentiation,	M15430
GO_Homophilic_Cell_Adhesion_Via_Plasma_Membrane_Adhesion_Molecules,	M15681
GO_Neuroepithelial_Cell_Differentiation,	M15104
GO_Membrane_Docking,	M11875
GO_Glial_Cell_Migration,	M14116

CNS Enrichment

Genes designated as enriched in the CNS were confirmed by the Human Protein Atlas v18 (www.proteinatlas.org) (Uhlén et al., 2015). Genes that were most highly expressed in the CNS (as described in the tissue tab under "Human Protein Atlas Information") were considered "CNS enriched." See below for direct access to the site.

Gene Name	URL (www.proteinatlas.org/)
NCAM1	ENSG00000149294-NCAM1/tissue
SPOCK1	ENSG00000152377-SPOCK1/tissue
EFNB3	ENSG00000108947-EFNB3/tissue
AKAP5	ENSG00000179841-AKAP5/tissue
SPTB	ENSG00000070182-SPTB/tissue
ENC1	ENSG00000171617-ENC1/tissue
FSTL4	ENSG00000053108-FSTL4/tissue
HEY1	ENSG00000164683-HEY1/tissue

Brain Region and Cell Type Enrichment Scores

The 30 most upregulated genes in the murine anterior cortex, striatum or cerebellum, as determined by fold change and significance, were obtained from Strand et al. (Strand et al., 2007). The median centered RNA-seq VST values of all 30 genes were extracted from our dataset and averaged for each sample to calculate the specific brain region enrichment scores. To calculate the enrichment score of the brain stromal astrocytes and microglia, the top 100 enriched genes for each cell type as determined by previously published data (Zhang et al., 2014) was utilized. Enrichment score was only calculated for forebrain regions as Zhang et al., 2014 determined cell type enrichment through processing of cortex tissue only. Enrichment score was analyzed as above. Significance was calculated by Student's t test.

Kaplan-Meier Curve for Brain Incidence

Specific cohorts of primary breast cancer patients (total tumors = 855) include EMC192 (GSE12276), EMC286 (GSE2034), MSK82 (GSE2603) and NKI295 (Bos et al., 2009; Minn et al., 2005; Wang et al., 2005). These cohorts were compiled in (Harrell et al., 2012) and normalized microarray data from this prior study was used to stratify tumors as either "high" or "low" based on their expression of the indicated gene and separated based on the median of gene expression. Brain incidence curves were generated using the R package "survival" (Therneau, 2000) available at https://cran.r-project.org/web/packages/survival/index.html and "survminer" available at https://cran.r-project.org/web/packages/survminer/index.html. Log-rank test was used to determine statistical significance.

QUANTIFICATION AND STATISTICAL ANALYSIS

Statistical analyses were performed using GraphPad Prism (version 7.0a). Data are represented by the mean ± SEM except when stated otherwise (Figures 1B and 1C). In all experiments "n" represents the number of biological replicates and includes either the tumor samples or monolayer samples analyzed. All tumor samples were collected from independent animals as stated in the Experimental Model and Subject Details section. p values were calculated by parametric, two-tailed Student's t test for all qRT-PCRs that were done to validate RNA-seq results and no assumptions were made. RPKM values were plotted as the $\log_2$RPKM and significance calculated by Student's t test. The exact values of "n" used are described in the corresponding figure legends.

DATA AND SOFTWARE AVAILABILITY

The complete computational analysis workflow is described in Figure S1 and is deposited on GitHub at https://github.com/zz2liu/bmx_seq.

The accession numbers for the BMX-seq raw data reported in this paper have been deposited under ID codes GSE115699, GSE115700, GSE115701, and the reference series GSE115702.

ADDITIONAL RESOURCES

We provide a web portal which includes BMX-sequencing analyses related to the transcriptomic profiles of brain metastases and the co-adaptation of surrounding brain stroma across disease models available at http://bmxexplorer.gotdns.org/.